

# 1

## Catalytic Hydrogen Production

*Xingyuan Gao and Sibudjing Kawi*

*National University of Singapore, Department of Chemical and Biomolecular Engineering, 4 Engineering Drive 4, 117585 Singapore, Singapore*

### 1.1 Introduction

Currently and in the near future, fossil fuels are/will be the major source of hydrogen production [1, 2]. As shown in Figure 1.1, almost all the industrial manufacturing processes for hydrogen rely on fossil fuels directly or indirectly [1]. Among the fossil fuels like coal, heavy hydrocarbons, and natural gas, methane is mostly studied due to its high abundance in the world, such as in the United States and Malaysia [4–8]. On the other hand, around 48% of hydrogen gas is generated from natural gas [9–11]. Moreover, methane is easy to handle and has a high H/C ratio [12]. Therefore, we focus on the thermocatalytic conversion of methane first in this part, followed by the conversion of other fossil fuels to produce hydrogen gas.

#### 1.1.1 Thermocatalytic Decomposition of Methane

Only hydrogen gas and carbon are produced in the thermal decomposition of hydrocarbons. This CO-free process is promising for industry [13, 14]. As the major component of hydrocarbons, methane has drawn much interest in the recent years in the production of hydrogen gas via thermal decomposition. The reaction mechanisms are shown below [9]. Initially, methane is chemisorbed on the exposed face of catalyst crystals; secondly, C—H bonds are broken in gaseous methane molecules to produce methyl groups and hydrogen atoms, followed by stepwise dissociations to generate  $\text{CH}_x$  and more hydrogen atoms; thirdly, two hydrogen atoms combine to generate hydrogen molecules, which are released in gaseous form; fourthly, atomic carbon aggregates and diffuses onto the surface of catalyst particles; fifthly, nucleation and growth of carbon filaments occur in the trailing face of catalyst particles.

Among several methane cracking technologies like plasma, pyrolytic, thermocatalytic, and photocatalytic routes, we focus on thermocatalytic decomposition due to the simultaneous formation of carbon nanofibers or carbon nanotubes

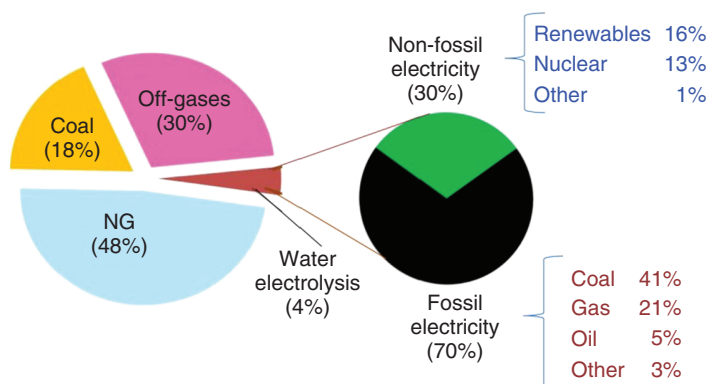


**Figure 1.1** The major sources of the industrial hydrogen manufacturing. Source: Reproduced with permission: © 2007, International Energy Agency [3].

that can be potentially used in various applications [14, 15]. Because of the very inactive C—H bond in methane molecules, the activation energy is high, and the reaction is strongly endothermic [16]. Therefore, catalysts are necessary to lower the reaction temperatures and promote the kinetics, including metal- and carbon-based catalysts [1].

#### 1.1.1.1 Metal Catalysts

Since the 1960s, transition metals (Ni, Fe, Co) have been extensively studied and show good catalytic performance in methane decomposition, which occurs at 500–800 °C, much lower than 1200 °C required without a catalyst [17–20]. However, the industrialization of this catalytic system is impeded due to the carbon deposits covering the active sites, leading to rapid deactivation [16, 21]. Modifications have been made to improve the reactivity and stability of transition metal-based catalysts using other transition metals and rare earth metals [22–26].

Bayat et al. [22] studied the Ni–Fe alloy derived from the reduction of the spinel  $\text{NiFe}_2\text{O}_4$  phase. Below 650 °C, the addition of Fe inhibited the encapsulation of carbon by facilitating the carbon diffusion. However, the active sites become fewer with increasing Fe content due to the lower degree of reducibility. To offset the negative effect of Fe, Bayat et al. [23] doped Cu into the Ni–Fe alloy to enhance the methane adsorption and Ni dispersion on alumina. The optimal ratio of Ni/Fe/Cu was 5 : 1 : 1.

Instead of adding Fe, Lua and Wang [24] doped Co into Ni–Cu to form a tri-metallic alloy. Since Co possesses a high melting point, the quasi-liquid phenomenon occurring between 650 and 775 °C was effectively inhibited, leading to enhanced stability. However, phase separation may be an issue with the further addition of Co. Following this work, a series of catalysts comprising Co and W in different ratios were developed [25]. When Co/W equaled 4 : 1, hydrogen gas and multiwall carbon nanotubes were simultaneously produced, showing the highest conversion of methane. It was found that non-interacted  $\text{Co}_3\text{O}_4$  was responsible for the superior catalytic performance.

Besides doping of transition metals, a series of rare earth metals were added to Ni to form bimetallic catalysts. Among the additives La, Sr, Nd, Pr, Y, and Sm, Ni-La

**Table 1.1** Summary of metal catalysts in methane decomposition.

Catalyst	Conditions	Findings	References
Ni-Fe/Al <sub>2</sub> O <sub>3</sub>	700 °C for 3 h; 30 vol% CH <sub>4</sub> and 70 vol% N <sub>2</sub> .	Fe inhibited the encapsulation of carbon by facilitating the carbon diffusion	[22]
Ni-Fe-Cu/Al <sub>2</sub> O <sub>3</sub>	700 °C for 3 h; 30 vol% CH <sub>4</sub> and 70 vol% N <sub>2</sub> .	Cu enhanced methane adsorption and improved the reducibility and nickel dispersion	[23]
Ni-Co-Cu	500–850 °C; 20 vol% CH <sub>4</sub> and 80 vol% N <sub>2</sub> .	The high melting point of Co inhibited the quasi-liquid phenomenon, leading to an enhanced stability	[24]
Co-W/MgO	700 °C; CH <sub>4</sub> at a flow rate of 50 sccm.	When Co/W equaled to 4 : 1; non-interacted Co <sub>3</sub> O <sub>4</sub> was responsible for the highest conversion of methane	[25]
Ni-La-Si	300~750 °C; CH <sub>4</sub> at a flow rate of 10 ml min <sup>-1</sup>	The high activity and low solid carbon formation were attributed to the good thermal stability and small Ni particle size	[26]

exhibited the highest activity and lowest solid carbon formation due to their good thermal stability and small Ni particle size [26] (Table 1.1).

#### 1.1.1.2 Carbon Catalysts

Due to the low cost, resistance to sulfur, and temperature, various carbon materials have been studied as alternatives to transition metals in methane decomposition [1, 16], including active carbon particles [27–30], ordered mesoporous carbons [31, 32], carbon black particles [33], and commercial carbon materials [34]. However, gradual deactivation occurred on carbon catalysts resulting from the coverage of inactive turbostratic carbon. To alleviate this issue, Muradov et al. [35] prolonged methane decomposition by generating active carbon aerosols continuously in a non-thermal plasma device. Besides, Dufour et al. [36] discovered that the addition of small amounts of oxidizing agents like oxygen, CO<sub>2</sub>, and steam in the feedstock could effectively enhance the sustainability. Furthermore, the gaseous form of carbon particles derived from partial gasification could inhibit the deactivation of catalyst in a fluid state and cyclic process between the reactor and heater [37].

#### 1.1.2 Partial Oxidation of Methane

Partial oxidation of methane (POM) has drawn much attention recently due to the compactness, good response time, and lower sensitivity to the type of fuels. In the

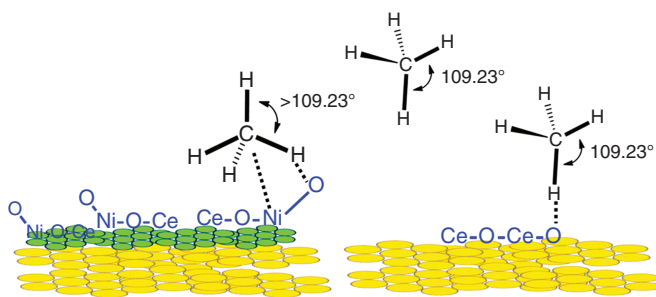
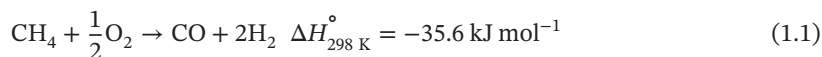


**Figure 1.2** Schematic representation of Ni/CeO<sub>2</sub> and CeO<sub>2</sub> surface having surface defects with under coordinated oxygen atoms. Source: Reproduced with permission from Pal et al. [40]; © 2015, American Chemical Society.

presence of oxygen, POM is considered as a fast and highly exothermic reaction to produce syngas as shown in Eq. (1.1) [38]:



The reaction can occur at a very high temperature without catalysts. However, the use of catalysts can lower the reaction temperature greatly that saves the energy input. The commonly studied catalysts for POM include noble transition metals, noble metals, and perovskites as shown in Table 1.2.

Amongst the transition metals, Ni with different supports is widely applied in POM. Pantaleo et al. [39] compared the catalytic performance of CeO<sub>2</sub> and La<sub>2</sub>O<sub>3</sub> single oxide supports and CeO<sub>2</sub>-La<sub>2</sub>O<sub>3</sub> mixed oxide supports prepared by wet impregnation and coprecipitation. Interestingly, coke only deposited on the single oxide supported catalysts. The enhanced anti-coking property of mixed oxide supported catalyst was attributed to the formation of a series of Ni-La<sub>2</sub>O<sub>3</sub> species with different oxidation states of Ni. Besides, in another study regarding Ni/CeO<sub>2</sub> [40], the surface and point defects with undercoordinated oxygen atoms in CeO<sub>2</sub> originating from the formation of O-Ni-O-Ce superstructures promoted the activation of C-H bonds (Figure 1.2). In addition to Ni-based catalysts, Co/ZrO<sub>2</sub> exhibited a very high conversion of methane and selectivity to hydrogen gas, out-performing many other catalysts [41].

Noble metals are also used in POM. A comparison among Pt, Pd, and bimetallic catalysts was conducted by Abbasi et al. [42]. It was found that Pd performed the best in this comparison, followed by the mixture and Pt alone. On the other hand, supports can also affect the performance of Rh-based catalysts [43]. Due to the oxygen spillover from Ce<sub>0.5</sub>Zr<sub>0.5</sub>O<sub>2</sub>, Rh was easily reoxidized and lost active sites; however, this spillover effect could be alleviated by Al<sub>2</sub>O<sub>3</sub>.

Perovskite structures present superior anti-coking properties due to the reaction of carbon deposits and oxygen species derived from the structure [60]. Sr<sub>0.8</sub>Ni<sub>0.2</sub>ZrO<sub>3</sub> exhibited a highly stable conversion of methane at 900 °C under a reducing atmosphere [44]. Similarly, LaGa<sub>0.65</sub>Mg<sub>0.15</sub>Ni<sub>0.2</sub>O<sub>3</sub> achieved 81% conversion of methane and 100% selectivity to hydrogen gas at 900 °C. This excellent catalytic property may be attributed to the existence of La<sub>2</sub>O<sub>3</sub> and La<sub>2</sub>O<sub>2</sub>CO<sub>3</sub> besides the perovskite structure [45].

**Table 1.2** Summary of catalysts in partial oxidation of methane.

Catalyst	Conditions	Findings	References.
Ni/CeO <sub>2</sub> -La <sub>2</sub> O <sub>3</sub>	700 °C; WHSV = 60 000; O/C = 0.5	Over 90% methane conversion; the formation of a series of Ni-La <sub>2</sub> O <sub>3</sub> species with different oxidation states of Ni inhibited cokes	[39]
Ni/CeO <sub>2</sub>	750 °C; WHSV = 50 000; O/C = 0.5	Over 85% methane conversion and 65% H <sub>2</sub> selectivity; the surface and point defects originated from the formation of O-Ni-O-Ce structures activated the C-H bonds	[40]
Co/ZrO <sub>2</sub>	800 °C; WHSV = 60 000; O/C = 0.5	Co/ZrO <sub>2</sub> exhibited 100% conversion of methane and 98.1% selectivity to hydrogen gas	[41]
Pd/γ-Al <sub>2</sub> O <sub>3</sub>	650 °C; WHSV = 38 400; O/C = 2	Pd performed the best (nearly 100%), followed by Pt-Pd and Pt alone	[42]
Rh/Al <sub>2</sub> O <sub>3</sub> and Rh/Ce <sub>0.5</sub> Zr <sub>0.5</sub> O <sub>2</sub>	600 °C; WHSV = 252 000; O/C = 2	Rh was easily reoxidized by oxygen spillover in Ce <sub>0.5</sub> Zr <sub>0.5</sub> O <sub>2</sub> ; this spillover effect could be alleviated by Al <sub>2</sub> O <sub>3</sub> , maintaining 60% methane conversion for 10 h	[43]
Sr <sub>0.8</sub> Ni <sub>0.2</sub> ZrO <sub>3</sub>	900 °C; WHSV = 66 000; O/C = 0.5	Over 94% methane conversion; a highly stable conversion of methane at 900 °C under reducing environment	[44]
LaGa <sub>0.65</sub> Mg <sub>0.15</sub> Ni <sub>0.20</sub> O <sub>3-δ</sub>	900 °C; WHSV = 3300; O/C = 0.5	81.2% methane conversion and 100% H <sub>2</sub> selectivity were attributed to the existence of La <sub>2</sub> O <sub>3</sub> and La <sub>2</sub> O <sub>2</sub> CO <sub>3</sub> besides the perovskite structure	[45]
Pt-NiO/Al <sub>2</sub> O <sub>3</sub>	800 °C; WHSV = 7200; O/C = 0.5	91.8% methane conversion and 98.4% H <sub>2</sub> selectivity; Ni reduction was promoted by Pt	[46]
Co/Al <sub>2</sub> O <sub>3</sub>	850 °C; WHSV = 60 000; O/C = 0.5	95% methane conversion and 93.6% H <sub>2</sub> selectivity were attributed to the formation of Co <sub>3</sub> O <sub>4</sub> as the major phase after 500 °C calcination	[47]
Ni/12CaO·7Al <sub>2</sub> O <sub>3</sub>	800 °C; WHSV = 30 000; O/C = 0.5	Over 90% methane conversion and 95% H <sub>2</sub> selectivity were attributed to the active oxygen ions and high dispersion of Ni.	[48]

**Table 1.2** (Continued)

Catalyst	Conditions	Findings	References.
Co/MgO	850 °C; WHSV = 20 000; O/C = 0.5	95% methane conversion, little coke formation, and sintering were attributed to small crystals embedded in the support derived from CoO–MgO solid solution	[49]
Ni/CeO <sub>2</sub> /Al <sub>2</sub> O <sub>3</sub>	800 °C; WHSV = 152 432; O/C = 0.5	Low loading of CeO <sub>2</sub> (1%) generated a highly dispersed CeO <sub>2</sub> particle, enhancing the reducibility and obtaining 80.3% methane conversion with less carbon deposition	[50]
Ni–Cr/Al <sub>2</sub> O <sub>3</sub>	700 °C; WHSV = 195 000; O/C = 0.5	85% methane conversion and enhanced stability were realized by the more dispersed Ni particles and surface basicity with addition of Cr	[51]
Ni–Rh/Al <sub>2</sub> O <sub>3</sub> –MgO	750 °C; WHSV = 354 044; O/C = 0.5	93% methane conversion and 95% H <sub>2</sub> selectivity; Rh prevented the oxidation of Ni	[52]
Rh/CeO <sub>2</sub>	700 °C; WHSV = 60 000; O/C = 0.5	The Rh ions in the surface lattice of CeO <sub>2</sub> were active in POM and obtained 95.2% methane conversion and 92.9% H <sub>2</sub> selectivity	[53]
Ni/ZrO <sub>2</sub> @SiO <sub>2</sub> core shell	750 °C; WHSV = 50 000; O/C = 0.5	Over 90% methane conversion and 75% H <sub>2</sub> selectivity were obtained with strong coke resistance due to the high oxygen storage capacity and steric hindrance	[54]
Ni/zeolite catalysts	750 °C; WHSV = 90 000; O/C = 0.5	100% methane conversion with strong anti-deactivation ability was attributed to less surface acidity and higher thermal stability	[55]
Ni/TiO <sub>2</sub>	800 °C; WHSV = 4800; O/C = 0.5	86.3% methane conversion and 99.7% H <sub>2</sub> selectivity were obtained, but serious deactivation was observed, resulting from the NiO and NiTiO <sub>3</sub> formation	[56]
LaCoO <sub>3</sub> /γ-Al <sub>2</sub> O <sub>3</sub>	800 °C; WHSV = 899 550; O/C = 0.25	Over 35% methane conversion and 40% H <sub>2</sub> selectivity; excellent stability was caused by highly dispersed Co and carbon removal by La <sub>2</sub> O <sub>3</sub>	[57]

**Table 1.2** (Continued)

Catalyst	Conditions	Findings	References.
$\text{La}_{0.08}\text{Sr}_{0.92}\text{Fe}_{0.20}\text{Ti}_{0.80}\text{O}_3$	900 °C; WHSV = 30 000; O/C = 0.5	Over 50% methane conversion and 60% H <sub>2</sub> selectivity; high oxygen vacancy concentration was responsible for the high activity	[58]
$\text{La}_{0.5}\text{Sr}_{0.5}\text{CoO}_3$	850 °C; WHSV = 30 000; O/C = 0.5	Over 70% methane conversion and 75% H <sub>2</sub> selectivity were realized with highly dispersed Co particles in the La <sub>2</sub> O <sub>3</sub> and SrO matrix	[59]

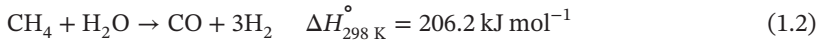
WHSV, weight hour space velocity (unit:  $\text{ml h}^{-1} \text{g}_{\text{cat}}^{-1}$ ); O/C, O<sub>2</sub>-to-carbon ratio.

### 1.1.3 Catalytic Reforming of Methane

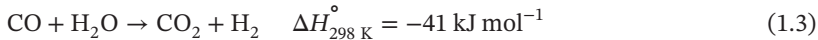
The popular syngas production methods consist of steam reforming of methane (SRM), oxidative steam reforming of methane (OSRM), and dry reforming of methane (DRM). The following will respectively introduce the reaction mechanism, issues to be overcome, and catalytic systems. Kinetic modeling will also be included.

#### 1.1.3.1 Steam Reforming of Methane (SRM)

SRM possesses many advantages, including high hydrogen yield and low cost to obtain hydrogen gas [61, 62]. The reaction equation is shown as below:



Due to the endothermic nature of this reaction, a high reaction temperature is preferred to generate a high yield of H<sub>2</sub> [63]. However, a simultaneous water-gas shift (WGS) reaction occurs, and the CO conversion is inhibited at high temperatures since WGS reaction is exothermic according to Eq. (1.3) [64]:



To solve this issue in industry, a two-reactor system has been adopted to achieve both a high conversion of methane and a high yield of H<sub>2</sub>. In detail, the reactants, methane and steam, are passed through the first reactor operated at 300–450 °C where the reaction is accelerated kinetically and more methane is converted thermodynamically according to Eq. (1.2) in spite of the low conversion of CO according to Eq. (1.3). Afterward, the intermediate products are continuously fed to the second low-temperature reactor (175–250 °C) with a high ratio of steam to convert more CO to form CO<sub>2</sub> and H<sub>2</sub> [65, 66].

To further purify or enhance the yield of hydrogen gas in the final products, CO<sub>2</sub> and H<sub>2</sub> is required to be removed *in situ* respectively by sorbents and selective membranes as shown in Figure 1.3 [67].

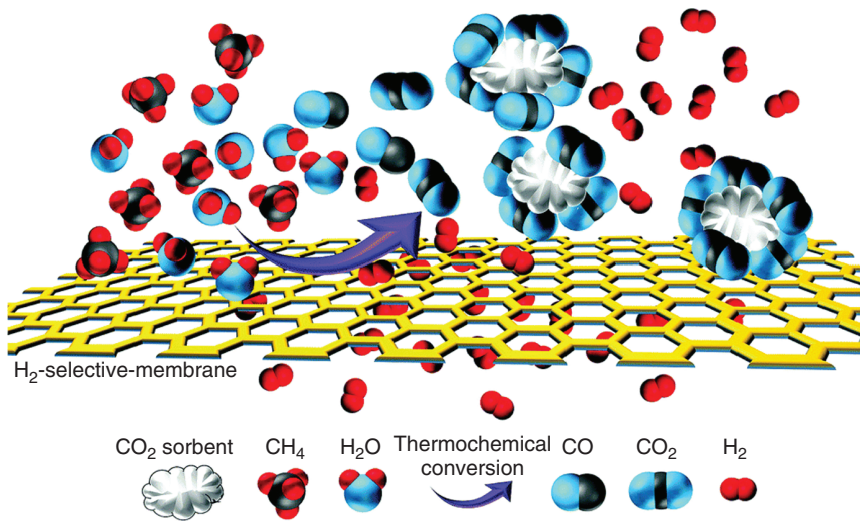


**Figure 1.3** Representation of  $H_2$  and  $CO_2$  removal by  $H_2$ -selective membranes and using  $CO_2$  sorbents. Source: Reproduced with permission from Ji et al. [67]; © 2018, The Royal Society of Chemistry.

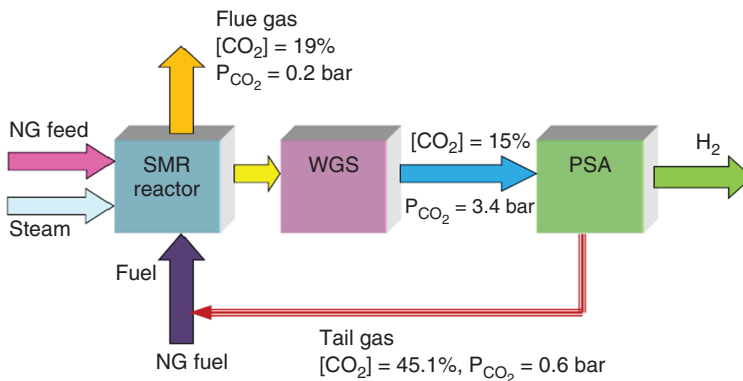


**Figure 1.4** Simplified block diagram of a modern SMR plant with major  $CO_2$  containing streams. SMR, steam methane reforming; WGS, water-gas shift reactor; PSA, pressure swing adsorption unit. Source: Reproduced with permission from Muradov [1]; © 2017, Elsevier.

Specifically for  $CO_2$  sorbents, different from the hot potassium carbonate or amine scrubber used about two to three decades ago, pressure swing adsorption (PSA), a physical adsorption technology, is widely adopted in modern SRM plants, achieving an ultrahigh purity of 99.999% for  $H_2$  (shown in Figure 1.4) [1]. In this process,  $CO_2$  is not selectively separated from other gases, but used together with  $CH_4$  and  $CO$  to provide heat for the reformer with  $CO_2$  as an exhaust vented out of the reactor system in the end [68].

Besides the design of the reactor system, SRM catalysts should possess the following stringent features: high catalytic stability, high conversion of methane, superior

mechanical strength, excellent thermal stability, low pressure drop, and good heat transfer [69]. Ni-based catalysts are commonly studied due to their high conversion and selectivity. However, carbon deposition hinders their large-scale application in industry. Additives and support materials have been used to alleviate this issue, including rare earth metals, noble metals, and perovskites as summarized in Table 1.3. For example, with the addition of Sn into Ni/YSZ, the activation energy of CH<sub>4</sub> increased, and the binding of carbon to the low-coordinated Ni sites was weakened, thus inhibiting the nucleation of carbon at Ni sites [78]. Similarly, Cu can potentially block the sites for carbon formation when forming Ni–Cu alloy, achieving 98% methane conversion and 99% H<sub>2</sub> selectivity [75]. When perovskite oxides were used as the supports or precursors, the catalytic stability could be enhanced, and coke formation could be diminished due to their high thermal stability under a wide range of oxygen partial pressures and also the formation of finely dispersed metal nanoparticles [60]. For example, La<sub>0.8</sub>Ce<sub>0.2</sub>Fe<sub>0.7</sub>Ni<sub>0.3</sub>O<sub>3</sub> exhibited stable catalytic performance regardless of the S/C ratio and only 0.2 wt% coke formed after a 20 hour test. This superior performance was attributed to the oxygen vacancy, which promoted the dissociation of steam and coke gasification [79]. Similarly, the lattice oxygen provided by LaAlO<sub>3</sub> and SrTiO<sub>3</sub> were located near the Ni surface, which migrated easily to the CH<sub>x</sub> fragments and oxidized the CH<sub>x</sub> [80].

In addition to the modifications mentioned above, preparation methods can also affect the physicochemical properties of Ni-based catalysts. For example, dielectric barrier discharge (DBD) was adopted together with the impregnation method in the preparation of Ni/SiO<sub>2</sub> catalysts, forming a smaller Ni particle size than that prepared with the conventional impregnation method [74]. For core–shell Ni–Al<sub>2</sub>O<sub>3</sub>/silicalite zeolite catalysts, repeated calcinations at elevated temperatures generated NiAl<sub>2</sub>O<sub>4</sub> spinel phase in the core, the catalytic performance of which was 10% higher than that prepared with traditional method [74]. Regarding Ni/CeO<sub>2</sub> catalysts, a hierarchical structure was formed with a template synthesis process, where the nanoporous and interwoven ceramic fiber template was loaded with NiO nanoparticles and supported on the CeO<sub>2</sub> scaffold. After thermal treatment, the microstructure of the nanocatalyst increased the conversion of methane up to 98% at 800 °C, which remained stable for five hours [81].

Besides Ni-based catalysts, noble metals with different supports have been tested in SRM. With ZrO<sub>2</sub> and Al<sub>2</sub>O<sub>3</sub> as mixed support materials, Pd–Rh metal foams presented excellent catalytic stability over 200 hours with little coke formation at 800 °C [70]. Ru also proved to be highly active and selective in SRM. By using  $\gamma$ -Al<sub>2</sub>O<sub>3</sub> as the support, the catalyst outperformed commercial Ni/Al<sub>2</sub>O<sub>3</sub> by 2 orders of magnitude for methane conversion. However, when the Ru loading was lower than 0.15 wt%, the oxidation of sub-nanometer Ru clusters caused a rapid decline in the conversion [71]. Despite the size limitations, Ru-based catalysts could maintain stable performance with a low S/C ratio (=1), while Ni/ $\alpha$ -Al<sub>2</sub>O<sub>3</sub> catalyst deactivated very rapidly when S/C = 2 [71]. Another noble metal, Pd, was found to be sensitive to the type of support material. Compared with Al<sub>2</sub>O<sub>3</sub>, La<sub>2</sub>O<sub>3</sub> promoted the formation of Pd<sup>0</sup>[Pd <sup>$\delta$ +</sup>O<sub>x</sub>La] species due to the metal–support interaction (MSI). La<sub>2</sub>O<sub>3</sub> could also enhance the interaction between Pt and Al<sub>2</sub>O<sub>3</sub> because of the improved thermal stability of Al<sub>2</sub>O<sub>3</sub> [72].

**Table 1.3** Summary of catalysts in steam reforming of methane.

Catalyst	Conditions	Findings	References
Pd–Rh/metal foam	300 °C; GHSV = 2000 h <sup>-1</sup> ; S/C = 2.5.	96.7% CH <sub>4</sub> conversion for 200 h was attributed to the absence of pore diffusion limitations, stable structure, and small loading of active metals	[70]
Ru/γ-Al <sub>2</sub> O <sub>3</sub>	600 °C; WHSV = 750; S/C = 1.	75% methane conversion and 68% H <sub>2</sub> selectivity; when the Ru loading was lower than 0.15 wt%, the oxidation of sub-nanometer Ru clusters caused the fast drop of the conversions	[71]
Pd/La <sub>2</sub> O <sub>3</sub> –Al <sub>2</sub> O <sub>3</sub>	510 °C; S/C = 3.	La <sub>2</sub> O <sub>3</sub> promoted the formation of Pd <sup>+</sup> [Pd <sup>δ+</sup> O <sub>x</sub> La] species and enhanced the interaction between Pt and Al <sub>2</sub> O <sub>3</sub>	[72]
Ni-nano-CaO/Al <sub>2</sub> O <sub>3</sub>	600 °C; WHSV = 2 700; S/C = 4.	86% methane conversion, 92% H <sub>2</sub> selectivity, and enhanced stability were attributed to high-temperature pretreatment and formation of Ca <sub>12</sub> Al <sub>14</sub> O <sub>33</sub>	[73]
Ni/SiO <sub>2</sub>	800 °C; WHSV = 24 000; S/C = 0.5.	Enhanced methane conversion was obtained by the smaller catalyst size prepared by dielectric barrier discharge (DBD) plasma	[74]
Ni–Cu/Al <sub>2</sub> O <sub>3</sub>	500 °C; WHSV = 2 000; S/C = 3.	Cu could possibly block the sites for carbon formation when forming Ni–Cu alloy, realizing over 85% methane conversion and 97% H <sub>2</sub> selectivity	[75]
Ni/Ce <sub>1-x</sub> Gd <sub>x</sub> O <sub>2</sub>	700 °C; WHSV = 560 000; S/C = 3.	75% methane conversion; Ga enhanced MSI so metal sintering was inhibited and carbon deposits were more reactive	[76]
Ru/MgO–Nb <sub>2</sub> O <sub>5</sub>	700 °C; WHSV = 20 000; S/C = 4.	Over 95% methane conversion, 72% H <sub>2</sub> selectivity; tetragonal Nb <sub>2</sub> O <sub>5</sub> and metallic Ru were formed <i>in situ</i> from amorphous niobic acid and Ru <sup>4+</sup> during the reaction	[77]

**Table 1.3** (Continued)

Catalyst	Conditions	Findings	References
Sn/Ni/YSZ	740 and 850 °C; S/C = 1.	The binding of carbon to the low-coordinated Ni sites was weakened with Sn addition, thus inhibiting the nucleation of carbon at Ni sites	[78]
La <sub>0.8</sub> Ce <sub>0.2</sub> Fe <sub>0.7</sub> Ni <sub>0.3</sub> O <sub>3</sub>	500–800 °C; WHSV = 108 000; S/C = 3.	Only 0.2 wt% coke formation after a 20 h test, which was attributed to the oxygen vacancy, promoting the dissociation of steam and coke gasification	[79]
Ni/LaAlO <sub>3</sub> and Ni/SrTiO <sub>3</sub>	800 °C; W/F = 1.58 g h mol <sup>-1</sup> . S/C = 2.	91.7% and 88.4% methane conversions with longer stabilities were achieved due to the lattice oxygen in perovskites, promoting the oxidation of CH <sub>x</sub> species	[80]

WHSV, weight hour space velocity (unit: ml h<sup>-1</sup> g<sub>cat</sub><sup>-1</sup>); S/C, steam-to-carbon ratio.

### 1.1.3.2 Oxidative Steam Reforming of Methane (OSRM)

OSRM is a combination of POM and SRM, which is also called autothermal reforming of methane. OSRM has the advantages of the heat generated from POM and hydrogen gas produced by SRM [82]. Compared with SRM, less methane is burnt, and thus the carbon efficiency is higher for OSRM [83]. Another merit of OSRM is that the process can be stopped and started rapidly, and the amount of hydrogen gas produced is large [38]. Owing to these advantages, OSRM is widely applied in the syngas production units in Fischer–Tropsch plants [84]. However, to reduce the carbon in the spent catalysts, an expensive process needs to run to separate C<sub>2+</sub> from methane [85]. Also, considering the high temperature of the burner, the high cost of operation is another concern [86]. To run the reaction properly, the S/C and O<sub>2</sub>/fuel ratios need to be controlled carefully to prevent the by-product formation, optimize the reaction temperature, and tune the gas compositions [82, 87, 88].

Due to the good activation of C—C bonds and low cost, Ni-based catalysts are widely studied for this reaction [38]. The MgAl<sub>2</sub>O<sub>4</sub> spinel material has been widely applied as the support material for Ni [84]. Besides, Ce–ZrO<sub>2</sub> mixed oxides have been popularly applied because of their high oxygen storage capacity (OSC). Together with the metal surface area of Ni, cubic phase Ce<sub>0.75</sub>Zr<sub>0.25</sub>O<sub>2</sub>-supported Ni catalyst exhibited high catalytic performance [89]. In detail, mobile oxygen species formed through a redox cycle inhibited coke deposition on the Ni active sites. As shown in Figure 1.5, a three-layer model was proposed comprising a layer of Ni–Ce–Zr–O<sub>x</sub> in the middle of free Ni metal and Ce–ZrO<sub>2</sub> support. The lattice oxygen consumed was replenished by the O<sub>2</sub> [90].

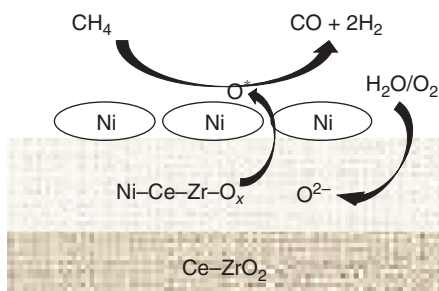


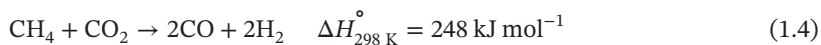
**Figure 1.5** Schematic of synthesis gas production over Ni/Ce-ZrO<sub>2</sub> catalyst. Source: Reproduced with permission from Roh et al. [90]: © 2001, Springer.

Several promoters were added to the above catalyst and Ag was shown to be better than Fe, Pt, and Pd due to its greater redox property. Compared with 0.1 wt%, higher loading of Ag (1 wt%) presented a higher reactivity [91]. Ce-ZrO<sub>2</sub> can also promote the catalytic properties of noble metals. The high reducibility and OSC enhanced the reactivity of Rh catalyst. Compared with mixed phase of Ce<sub>0.5</sub>Zr<sub>0.5</sub>O<sub>2</sub>, single cubic phase led to superior performance [92]. Similar effect was exerted on Pt catalyst, where the carbon deposits were continuously removed at the metal-support interface due to the OSC of the Ce<sub>0.5</sub>Zr<sub>0.5</sub>O<sub>2</sub> support [93]. When Ce-ZrO<sub>2</sub> was adopted as the support, the addition of Al<sub>2</sub>O<sub>3</sub> could enhance the metal dispersion and reduce the size of particles. Besides the carbon inhibition effect, Zr in the support could prevent the formation of inactive NiAl<sub>2</sub>O<sub>4</sub> [94, 95].

Different opinions existed that considering the high reaction temperature, deactivation or poisoning of the catalysts in OSRM may not be as serious as the catalysts in steam reforming. Therefore, instead of focusing on the catalyst design, however, more attention should be paid to the optimization of pellet shape and minimizing the pressure drop [84].

### 1.1.3.3 CO<sub>2</sub>/Dry Reforming of Methane

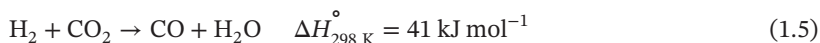
Among the two greenhouse gases – methane and CO<sub>2</sub> – though the concentration of methane is much lower than that of CO<sub>2</sub>, methane's global warming potential is 28–36 times higher than CO<sub>2</sub>. DRM can effectively reduce these greenhouse gases [96, 97]. Besides, syngas (mixture of CO and H<sub>2</sub>) as the product of this reaction acts as both a sustainable fuel alternative to fossil fuel and a precursor to produce high value-added chemicals such as ammonia and methanol [98–105]. The main reaction equation is shown below:



The Fischer-Tropsch reaction will be benefited from this low H<sub>2</sub>/CO ratio because of the suppression of methanation and the promotion of chain growth. In addition, the endothermic nature promotes the Solchem process since solar energy is converted to chemical energy. Furthermore, the storage of seasonal energy is applicable in the form of H<sub>2</sub> and CO [106–111]. In the long term, however, a more sustainable way to supply the heat for DRM reaction is to use renewable energy [112].

Based on the stoichiometry in Eq. (1.4), the conversion of CH<sub>4</sub> and CO<sub>2</sub> will be equal. Considering the reverse WGS reaction as shown in Eq. (1.5), more CO<sub>2</sub> will

be converted to form CO and water; thus generally CO<sub>2</sub> conversion should be higher than that of methane [112, 113]. In terms of the yield of H<sub>2</sub>, however, this side reaction needs to be inhibited:



In spite of the environmental and economic potential, DRM is still industrially immature because of the relatively high cost and problems related to the development of robust catalysts with a long lifespan. Especially for the catalyst design, two factors hinder the large-scale applications in industry: coke formation based on Eqs. (1.6, 1.7) and metal sintering at high temperatures [112–117]. Therefore, it is crucial to develop a highly active and stable catalyst with economic feasibility and excellent anti-deactivation ability [112]:



The commonly investigated catalysts include noble metals and non-noble metals. Noble metals such as Pt, Pd, and Rh exhibit outstanding catalytic performance [118]. In the catalytic tests of a series of noble metals, the order of the activity was found to be Rh, Ru > Ir > Pd, Pt. Ru and Rh performed better than other noble metals, and in industry, Ru may be more suitable considering its lower cost than that of Rh. The high activity and coke resistance derived from the dissociation of CO<sub>2</sub> to form CO and O species that subsequently activated methane molecules and oxidized CH<sub>x</sub> species to prevent the carbon deposition [119]. In another study regarding the support effect on Pt catalysts, Pt/TiO<sub>2</sub> and Pt/ZrO<sub>2</sub> exhibited long-term stability with negligible coke formation during 80 hours on stream. The excellent performance of Pt/TiO<sub>2</sub> was attributed to the coverage of TiO<sub>x</sub> on the surface of Pt, which prevented the growth of Pt nanoparticles. It was reported that small Pt particles inhibited both CO and methane dissociation, thus reducing carbon formation on the metal surface [120–122]. A similar mechanism was speculated to occur for Pt/ZrO<sub>2</sub>. Besides, the strong Pt–Zr interaction inhibited coke formation by blocking the active sites [123, 124]. In the absence of this strong interaction, Pt/Cr<sub>2</sub>O<sub>3</sub> and Pt/SiO<sub>2</sub> deactivated rapidly [125].

Despite the high activity and coke resistance for noble metals, their application is hindered by their high cost and also the occurrence of metal sintering [104]. Ni and Co catalysts are proven to be the most suitable candidates considering their high intrinsic activity and affordable cost [104, 126]. Co-based catalysts have been investigated based on the interaction with different supports. Due to the strong sintering of SrO and BaO, Co active sites were covered and exhibited very low activity. Although the initial conversions were acceptable for SiO<sub>2</sub>-, CaO-, and Al<sub>2</sub>O<sub>3</sub>-supported Co catalysts, deactivation was rapid. With MgO as the support, activity, stability, and anti-sintering properties were enhanced up to 50 hours, which might be caused by the strong interaction between CoO and MgO and low reducibility of the catalyst [127, 128].

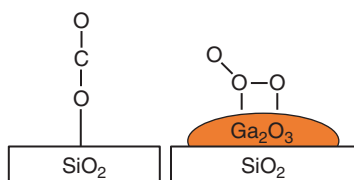


**Figure 1.6** Activation of  $\text{CO}_2$  on  $\text{Ga}_2\text{O}_3$ -promoted  $\text{SiO}_2$  support. Source: Reproduced with permission from Pan et al. [138]; © 2010, The Royal Society of Chemistry.

Compared with Co and noble metals, Ni-based catalysts are more widely studied due to their low cost and good activity [104]. However, metal sintering and coke formation impede further application in industry. In the following section, catalyst design will be introduced based on surface regulation, oxygen defects, interfacial engineering, and structural optimization.

**Surface Regulation** In the DRM reaction,  $\text{CO}_2$  and  $\text{CH}_4$  are adsorbed, dissociated, and recombined to form CO and  $\text{H}_2$  on the catalyst surface. Modifications of the surface acidity and basicity exert great effects on performance and coke resistance [104].

It was reported that Lewis acidic sites could balance the removal of carbon and the activation of  $\text{CH}_4$ , thus inhibiting the coke formation and improving stability [129]. Also, surface basicity could dissociate  $\text{CO}_2$  to form CO and O species that oxidized  $\text{CH}_x$  to form CO and  $\text{H}_2$  [104]. To enhance the surface basicity, alkali metals, alkali earth metals, and rare earth metal oxides have been investigated [104, 130–133].

Rare earth metal oxide  $\text{La}_2\text{O}_3$  promoted the adsorption of  $\text{CO}_2$  to form La oxycarbonate ( $\text{La}_2\text{O}_2\text{CO}_3$ ) [134], which subsequently reacted with  $\text{CH}_4$  molecules to produce CO and prevented coke formation based on the *in situ* DRIFT study [135]. MgO could further enhance the surface basicity of Ni/ $\text{La}_2\text{O}_3$  catalyst so that more  $\text{CO}_2$  adsorption occurred and monoclinic  $\text{La}_2\text{O}_2\text{CO}_3$  was formed by reacting with  $\text{La}_2\text{O}_3$ . This monoclinic phase reacted more efficiently with carbon deposits than hexagonal  $\text{La}_2\text{O}_3$  and  $\text{La}_2\text{O}_2\text{CO}_3$  mixtures produced with a low Mg/La ratio [136]. The promotional effect of  $\text{La}_2\text{O}_3$  is derived from the oxygen atoms of  $\text{La}_2\text{O}_2\text{CO}_3$  that could react with CH and C species, while La–Ni accelerated the dissociation of C–H bond and intensified the coke formation. In summary, La metal dopant was not effective as its oxide [137].

In addition to  $\text{La}_2\text{O}_3$  and MgO, the enhanced surface basicity of Ni/ $\text{SiO}_2$  catalyst was achieved by doping with  $\text{Ga}_2\text{O}_3$ , leading to greater carbonate or bicarbonate formation along with the  $\text{CO}_2$  adsorption as shown in Figure 1.6. The coke formed on the  $\text{SiO}_2$  surface reacted more easily with the carbonate species than the physically or linearly adsorbed  $\text{CO}_2$  [138].

In some circumstances, however, if the surface basicity is too strong, more coke deposits will generate due to less  $\text{CO}_2$  adsorption [139]. In this case,  $\text{Y}_2\text{O}_3$  was doped to offer weak and medium basic sites, leading to a higher activity and stability than pristine MgO/ $\text{Al}_2\text{O}_3$  [140].

Besides the surface basicity, the concentration of surface hydroxyl groups can affect the oxidation of carbon deposits. The addition of  $\text{B}_2\text{O}_3$  into Ni/ $\text{Al}_2\text{O}_3$  can effectively increase the amount of hydroxyl groups on the surface, thus inhibiting the coke formation [141].

**Oxygen Defects** The generation of oxygen defects influences the oxygen mobility, thus determining the carbon resistance of the Ni-based catalysts [104]. Several promoters can form the oxygen defects, including rare earth metal oxides, transition metal oxides, mixed oxides, and perovskite oxides.

As representative of rare earth metal oxides, CeO<sub>2</sub> can produce lattice oxygen defects and promote surface oxygen mobility, thus scavenging carbon species. Typically, the reversible conversion of Ce<sup>4+</sup> and Ce<sup>3+</sup> determined the formation of oxygen defects, enhancing the adsorption of CO<sub>2</sub> or O<sub>2</sub> molecules that oxidized the surface coke and maintained the active metal sites. However, excessive doping of CeO<sub>2</sub> may block the access of reactant molecules and decrease conversion [104, 113, 142, 143].

The activation sites for CH<sub>4</sub> and CO<sub>2</sub> were investigated in a theoretical study as demonstrated in Figure 1.7. In detail, CH<sub>4</sub> molecules were preferably activated on the oxygen vacancies at the metal–support interfaces, metal vacancies, and metal–support interfaces. For CO<sub>2</sub>, oxygen vacancies on the support or metal–support interfaces were more available for the activation of the molecules. Moreover, the interfacial oxygen of CeO<sub>2</sub> could regenerate the active sites. It can be seen that oxygen vacancies played a dominant role in both CH<sub>4</sub> and CO<sub>2</sub> activation [144].

ZrO<sub>2</sub> can further enhance the oxygen vacancy concentration when added to CeO<sub>2</sub>. The cubic phase of Ce<sub>x</sub>Zr<sub>1-x</sub>O<sub>2</sub> exhibited a higher OSC and oxidized the carbon more easily to form CO [145]. Interestingly, the loading of Ni in this mixed oxide also affected the oxygen vacancy concentration. With a 9.3 mol% Ni amount, CH<sub>4</sub> and CO<sub>2</sub> were converted with a higher percentage than other ratios [146].

Another two rare earth metal oxides, Y<sub>2</sub>O<sub>3</sub> and La<sub>2</sub>O<sub>3</sub>, were also applied as the support to adjust the oxygen vacancy.  $\alpha$ -Oxygen derived from Y<sub>2</sub>O<sub>3</sub> presented very effective activation of CH<sub>4</sub> and removal of carbon. However, a small amount of oxygen may be fed considering the limited concentration of  $\alpha$ -oxygen. For La<sub>2</sub>O<sub>3</sub>, oxycarbonate formation could adsorb more CO<sub>2</sub> while the addition of Sr could further enhance the oxygen vacancy concentration and oxidize the coke more effectively [147, 148].

Similarly to the rare earth metal oxides, transition metal oxides like ZrO<sub>2</sub> and TiO<sub>2</sub> could also provide oxygen vacancies because of their incompletely occupied *d* orbitals [149–152]. Due to the strong interaction between Ni and ZrO<sub>2</sub>, CH<sub>x</sub> originated from the CH<sub>4</sub> activation could be effectively converted to CO and H<sub>2</sub> by reacting with the lattice oxygen in ZrO<sub>2</sub>. Moreover, CO<sub>2</sub> adsorption was promoted by the oxygen defects, thus inhibiting the coke formation [153]. Similarly, two types of oxygen species were observed in TiO<sub>2</sub>, i.e. the lattice oxygen in the interface and oxygen ions inside TiO<sub>2</sub>. The lattice oxygen could react with the coke on the surface of Ni to form CO and regenerated Ni for the continuous conversion [149].

Different from rare earth metal and transition metal oxides, perovskite oxides with ABO<sub>3</sub> structure generated oxygen defects by lattice distortions. The promoted oxygen fluidity enhanced the catalytic performance in DRM reaction [154–156]. A variety of elements have been used to substitute the A or B sites to form lattice defects [157–160]. When La was used in the A-site, Sr and Ce were doped to enhance the

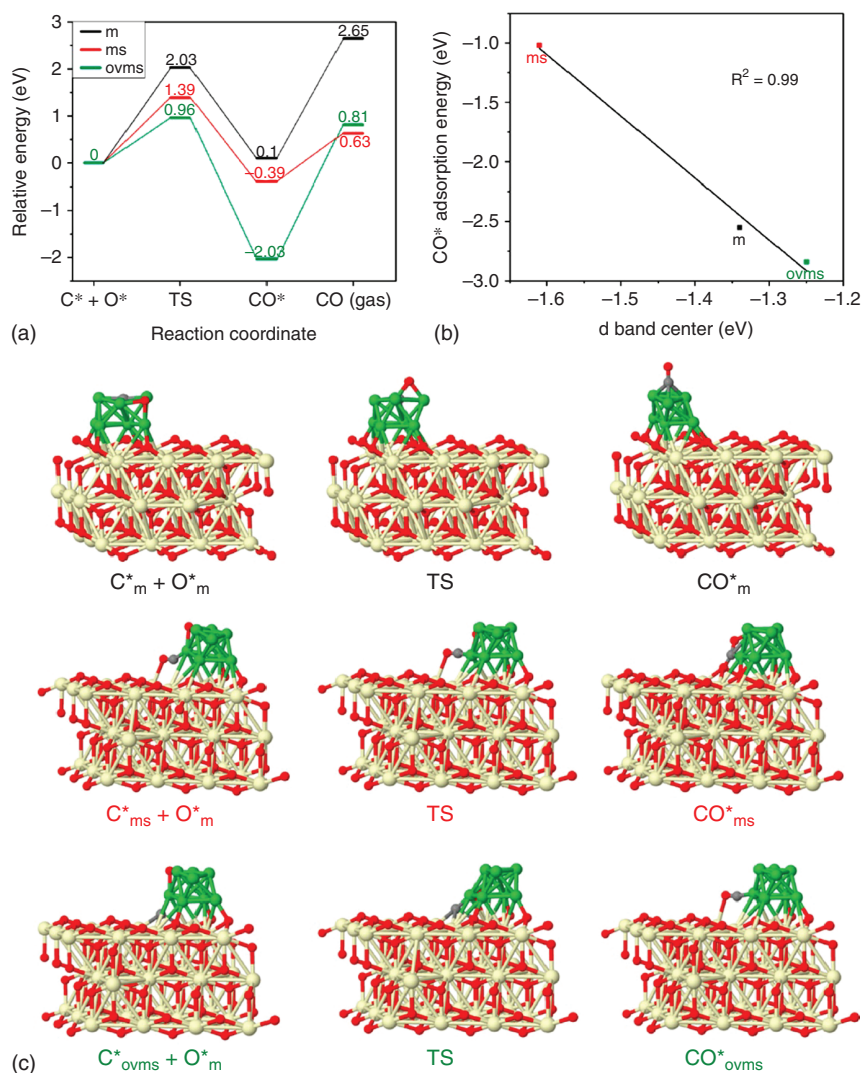


**Figure 1.7** Three paths of C\* elimination. (a) Relative energy of C\* elimination at m, ms, and ovms sites. (b) Relation of d band center with CO\* adsorption energy. (c) Corresponding configurations of part a. Gray spheres represent C, red spheres represent O, green spheres represent Ni, and cream-colored spheres represent Ce. Source: Reproduced with permission from Lian et al. [144]: © 2020, American Chemical Society.

oxygen vacancies in the LaNiO<sub>3</sub> perovskite structure. Due to the different oxidation states and size of Sr and La ions, lattice distortions occurred, and oxygen vacancies were generated. Differently, Ce<sup>3+</sup> and La<sup>3+</sup> have the same valence state, while the oxygen vacancies were derived from local redox fluctuations of Ce ions. For B-site replacement, Cu and Fe both promoted the formation of oxygen vacancies. However, Ni agglomeration occurred with copper substitution, while for Fe-substituted Ni perovskite, higher stability was accomplished due to the stronger MSI [160].

**Interfacial Engineering** The interfacial engineering for both Ni-metal and Ni-support interfaces influences the electron density, metal dispersion, and surface composition, thus affecting the reactant activation and catalyst deactivation behavior [161, 162]. When Cu formed a Ni–Cu alloy with Ni, the environment of Ni was changed, and coke formation was prevented [163]. A similar effect was observed for Ni–Co alloy catalysts [164]. When noble metals were doped to form alloys with Ni, metal dispersion was enhanced, and the oxidation of  $\text{CH}_x$  species was promoted instead of dehydrogenation [165, 166].

Besides the strategy to tune the alloy interface, the modification of MSI can determine the size, dispersion, surface area, and reducibility. For the inert  $\text{SiO}_2$  support, the formation of Ni phyllosilicate was promising to enhance the MSI. Several methods were used to prepare the phyllosilicate structure, such as ammonia evaporation and sequential two-step calcination [167, 168]. Compared with the inert  $\text{SiO}_2$ , basic support  $\text{MgO}$  or  $\text{MgAl}_2\text{O}_4$  could produce highly dispersed Ni nanoparticles with  $\text{CO}_2$  adsorptions. However, too strong MSI may lead to the metal sintering at a high reduction temperature [169–171]. Besides the inert and basic oxides,  $\text{CeO}_2$  can form Ni–Ce solid solutions, which changed the electronic or chemical state of Ni and adsorbed  $\text{CH}_4$  by both Ni and O atoms, thus inhibiting carbon formation, proven by the lack of C or  $\text{NiC}_x$  peaks as shown in Figure 1.8 [142].

**Structural Optimization** Both porous materials and hierarchical structures can prevent the Ni sintering at high temperatures [101, 104, 105]. Porous carbon support synthesized from renewable hydrochar effectively anchored the  $\text{Ni}^{2+}$  ions on the surface, controlling the average diameter of Ni particles within 8 nm. Mesoporous active carbon with mesopores and high surface area provided strong MSI and enhanced the methane conversion [172, 173]. Similarly, with ordered structures and high porosities, porous silica materials are also applied as supports to control the Ni dispersion [174–179]. With the help of amine groups of polyethylenimine (PEI), SBA-15 with ordered channels and surface silanol groups could trap Ni ions by physical confinement effect and chemical bonding (Figure 1.9) [176].

Other metal oxides with mesoporous structures also draw attention due to their multifunctional nature [180–183]. For example, NiO–MgO– $\text{Al}_2\text{O}_3$  mesoporous frameworks provided both the mesopores to anchor the active metals and prevent sintering and the basic sites to adsorb more  $\text{CO}_2$  to form CO and O radicals, thus removing coke on the metal surface [180]. In another case of mesoporous NiO– $\text{CeO}_2$ – $\text{Al}_2\text{O}_3$  material, the only difference was apparent in the redox property offered by  $\text{CeO}_2$  that oxidized the coke instead of by the basic nature of  $\text{MgO}$  [184].

In addition to the usage of porous support, architecture designs of catalysts also alleviate metal sintering and coke formation. Following the first core–shell nanoreactor Pt@CoO, various nanostructures have been developed recently to control metal distribution and enhance the dispersion [104, 185–193].

Ni@ $\text{SiO}_2$  core–shell structures have been widely studied in the DRM reaction. When a thick shell of silica was used, the core–shell structure was transformed into

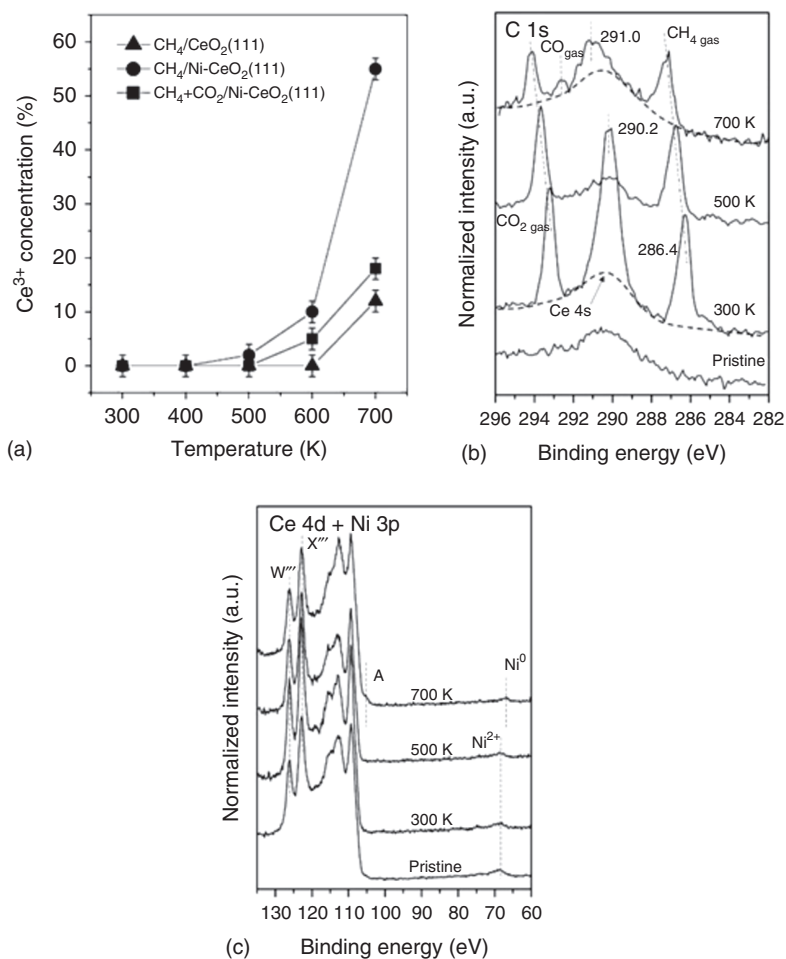


**Figure 1.8** (a) Ce<sup>3+</sup> concentration measured in XPS as a function of temperature under reaction conditions (i.e. exposure to 100 mTorr of methane or a mixture of 100 mTorr of methane and 100 mTorr of CO<sub>2</sub>). (b) and (c) C 1s and Ce 4d + Ni 3p spectra of the Ni-CeO<sub>2</sub>(111) ( $\theta_{\text{Ni}} \approx 0.1$  ml) surface under 100 mTorr CH<sub>4</sub> + 100 mTorr of CO<sub>2</sub> at 300, 500, and 700 K. Source: Reproduced with permission from Liu et al. [142]; © 2016, Wiley.

a yolk-shell structure with Ni metal as the core surrounded by Ni embedded in the SiO<sub>2</sub> shell (Figure 1.10). The excellent conversion and stability were attributed to the small satellite Ni particles and the strong MSI [194].

To further enhance the catalytic performance, Ni-Mg phyllosilicate was adopted as the shell to provide strong MSI, basicity, and modified pore structures. With this synergistic effect, both Ni sintering and coke formation were inhibited [195, 196]. Similarly, NiMgAl layer double hydroxide was prepared first, followed by being coated with another mesoporous silica layer. After thermal treatment, Ni metal was confined by MgO and SiO<sub>2</sub>, leading to suppressed carbon deposition [197] (Table 1.4).

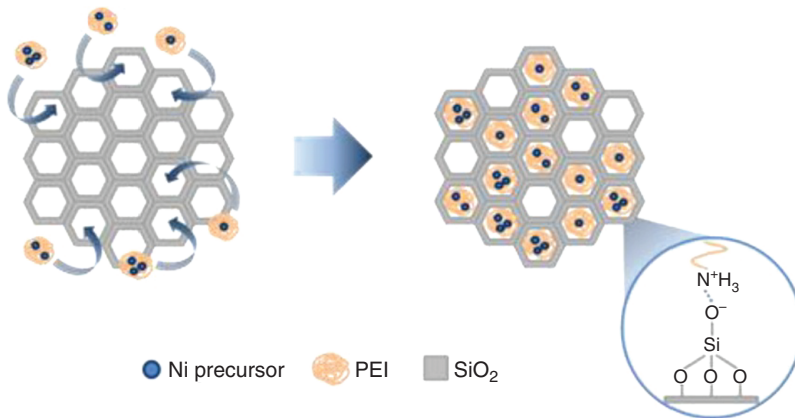


**Figure 1.9** Schematic diagram of PEI-aided route. Source: Reproduced with permission from Kang et al. [176]: © 2017, Elsevier.

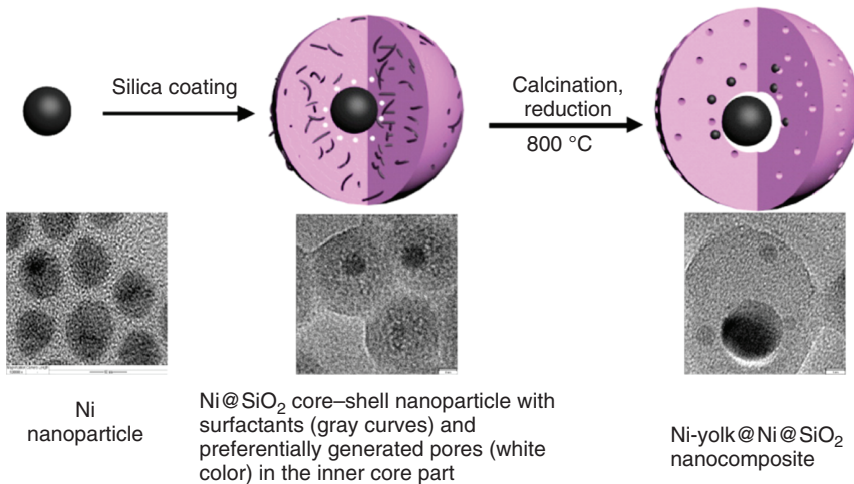


**Figure 1.10** Schematic illustration of the formation process of Ni-yolk@Ni@SiO<sub>2</sub> nanocomposite. Source: Li et al. [194]/with permission of American Chemical Society.

#### 1.1.4 Thermocatalytic Conversion of Other Fossil Fuels

According to US DOE, 95% of the overall hydrogen production was based on fossil fuels [2]. Besides the methane reforming discussed above, catalytic steam reforming of LPG was studied as another way to generate hydrogen gas. Noble metal catalysts were mainly investigated with oxides as the supports. When Ru/CeO<sub>2</sub>-Al<sub>2</sub>O<sub>3</sub> was applied, the products were mainly H<sub>2</sub>, CO, and CO<sub>2</sub> while the decomposition of LPG and methanation were responsible for methane, ethane, and ethylene production [198]. Addition of oxygen was effective in the elimination of higher hydrocarbons, reduction of coke, and enhancement of stability [199, 200]. Besides Ru, other noble metals such as Pd, Rh, and Pt exhibited good anti-coking ability in steam reforming of LPG [201, 202].

**Table 1.4** Summary of catalysts in dry reforming of methane.

Catalyst	Conditions	Findings	References
Ru/MgO–Al <sub>2</sub> O <sub>3</sub>	500 and 650 °C; CO <sub>2</sub> /CH <sub>4</sub> = 4.	The dissociation of CO <sub>2</sub> to form CO and O species that subsequently activated methane molecules and oxidized CH <sub>x</sub> species to prevent the carbon deposition	[119]
Pt/ZrO <sub>2</sub>	600 °C; CO <sub>2</sub> /CH <sub>4</sub> = 1	The strong Pt–Zr interaction inhibited coke formation by blocking the active sites	[123]
Ni/La <sub>2</sub> O <sub>3</sub>	700 °C; CH <sub>4</sub> /CO <sub>2</sub> = 1	70% CH <sub>4</sub> and 75% CO <sub>2</sub> conversion; La oxycarbonate reacted with carbon to form CO	[134]
Ni/MgO–La <sub>2</sub> O <sub>3</sub>	700 °C; CH <sub>4</sub> /CO <sub>2</sub> = 1	63% CH <sub>4</sub> and 65% CO <sub>2</sub> conversion; more CO <sub>2</sub> adsorbed on the surface with MgO	[136]
Ni/SiO <sub>2</sub> –Ga <sub>2</sub> O <sub>3</sub>	700 °C; CH <sub>4</sub> /CO <sub>2</sub> = 1	70% CH <sub>4</sub> and 79% CO <sub>2</sub> conversion; carbonate or bicarbonate was formed by CO <sub>2</sub> adsorption promoted by Ga <sub>2</sub> O <sub>3</sub>	[138]
HTNi–Y	700 °C; CH <sub>4</sub> /CO <sub>2</sub> = 1	74% CH <sub>4</sub> and 78% CO <sub>2</sub> conversion; weak and medium basic sites were introduced to the surface by addition of Y <sub>2</sub> O <sub>3</sub>	[140]
5%Ni/B <sub>2</sub> O <sub>3</sub> –Al <sub>2</sub> O <sub>3</sub>	700 °C; CH <sub>4</sub> /CO <sub>2</sub> = 1	75% CH <sub>4</sub> and 67% CO <sub>2</sub> conversion; more hydroxyl groups were formed on borated surface, oxidizing the carbon	[141]
NiRhCe <sub>2</sub> Zr <sub>1.51</sub>	700 °C; CH <sub>4</sub> /CO <sub>2</sub> = 7 : 3	16% CH <sub>4</sub> and 37.5% CO <sub>2</sub> conversion; more oxygen vacancies were generated by the cubic phase of Ce <sub>x</sub> Zr <sub>1-x</sub> O <sub>2</sub>	[145]
Ni–SDL (Sr doped La)	600 °C; CH <sub>4</sub> /CO <sub>2</sub> = 1	78% CH <sub>4</sub> and 60% CO <sub>2</sub> conversion; surface oxygen species mobility was enhanced by Sr	[148]
Ni–CaO–ZrO <sub>2</sub>	700 °C; CH <sub>4</sub> /CO <sub>2</sub> = 1	73% CH <sub>4</sub> and 83% CO <sub>2</sub> conversion; CH <sub>x</sub> species on Ni surface reacted with the lattice oxygen in ZrO <sub>2</sub> to form CO and H <sub>2</sub>	[153]
La <sub>0.8</sub> Sr <sub>0.2</sub> Ni <sub>0.8</sub> Cu <sub>0.2</sub> O <sub>3</sub>	600–800 °C; CH <sub>4</sub> /CO <sub>2</sub> = 1	80% CH <sub>4</sub> and 80% CO <sub>2</sub> conversion; lattice oxygen mobility was promoted with the addition of Sr and Cu	[160]
NiPt/Al <sub>2</sub> O <sub>3</sub>	700 °C; CH <sub>4</sub> /CO <sub>2</sub> = 1	85.8% CH <sub>4</sub> and 91.2% CO <sub>2</sub> conversion; CH was oxidized by Pt layer in the core–shell structure	[166]

Table 1.4 (Continued)

Catalyst	Conditions	Findings	References
Ni@Ni embedded SiO <sub>2</sub>	700 °C; CH <sub>4</sub> /CO <sub>2</sub> = 1	74% CH <sub>4</sub> and 82% CO <sub>2</sub> conversion; interaction with SiO <sub>2</sub> and dispersion of Ni were both enhanced by phyllosilicate	[167]
Ni/SiO <sub>2</sub>	700 °C; CH <sub>4</sub> /CO <sub>2</sub> = 1	80% CH <sub>4</sub> and 85% CO <sub>2</sub> conversion; metal dispersion and metal–support interaction were enhanced by sequential calcination	[168]
AuNi/MgAl <sub>2</sub> O <sub>4</sub>	650 °C; CH <sub>4</sub> /CO <sub>2</sub> = 69 : 30	20% CH <sub>4</sub> and 48% CO <sub>2</sub> conversion; MgAl <sub>2</sub> O <sub>4</sub> spinel phase enhanced the surface basicity and CO <sub>2</sub> adsorption, thus inhibiting the coke formation	[171]
Ni/CeO <sub>2</sub>	450 °C; CH <sub>4</sub> /CO <sub>2</sub> = 1	10 <sup>-7</sup> Torr CH <sub>4</sub> and 10 <sup>-7</sup> Torr CO <sub>2</sub> ; Ni–Ce solid solution promoted the adsorption of CH <sub>4</sub> on Ni and O	[142]
Ni@C	700 °C; CH <sub>4</sub> /CO <sub>2</sub> = 1	68% CH <sub>4</sub> and 80% CO <sub>2</sub> conversion; Ni dispersion was enhanced due to the confinement effect of pore structure	[172]
Ni/SBA-15	750 °C; CH <sub>4</sub> /CO <sub>2</sub> = 1	85% CH <sub>4</sub> and 88% CO <sub>2</sub> conversion; the steric hindrance of ordered channels inhibited the metal sintering	[176]
NiO–MgO–Al <sub>2</sub> O <sub>3</sub>	700 °C; CH <sub>4</sub> /CO <sub>2</sub> = 1	78% CH <sub>4</sub> and 83% CO <sub>2</sub> conversion; coke formation and metal agglomeration were alleviated by the pore structure and enhanced basicity	[180]
NiO–CeO <sub>2</sub> –Al <sub>2</sub> O <sub>3</sub>	700 °C; CH <sub>4</sub> /CO <sub>2</sub> = 1	78% CH <sub>4</sub> and 73% CO <sub>2</sub> conversion; thermally stable mesoporous support confined Ni in the matrix and redox CeO <sub>2</sub> prevented coke formation	[184]
Ni@SiO <sub>2</sub>	800 °C; CH <sub>4</sub> /CO <sub>2</sub> = 1	90% CH <sub>4</sub> and 95% CO <sub>2</sub> conversion; small satellite Ni particles and strong metal–support interaction enhanced the catalytic performance with appropriate shell thickness	[194]
NiMgAl–(LDH)@mesoporous–SiO <sub>2</sub>	750 °C; CH <sub>4</sub> /CO <sub>2</sub> = 1	79% CH <sub>4</sub> and 88% CO <sub>2</sub> conversion; MgO and SiO <sub>2</sub> layers confined Ni particles in the cavity	[197]

However, considering the high cost of raw materials, noble metals may not be suitable candidates for commercial use. Due to the high OSC, redox property, and strong metal–support interaction, CeO<sub>2</sub>-based catalysts are promising alternatives [201–207]. Compared with traditional Ni/Al<sub>2</sub>O<sub>3</sub>, the redox property of CeO<sub>2</sub> prepared with the surfactant-assisted approach presented excellent activity and coke resistance.

In addition to steam reforming, dry reforming of hydrocarbons draws attention since it can alleviate the greenhouse gas effect. For dry reforming of ethane, with the increase of Mn concentration, the conversion of ethane increased accordingly. When  $\text{SiO}_2$  was replaced by  $\text{Al}_2\text{O}_3$ , the conversion of ethane increased while the yield of ethylene decreased. To obtain a higher selectivity to ethylene, the  $\text{CO}_2$ /ethane ratio should be kept at a high value [208]. When Rh/ZSM-5 was adopted as the catalyst, the reaction rate of dry reforming of ethane was five times higher than DRM, which may be attributed to the easier dissociation of the C—H bond in ethane than methane. However, the coke formation was considerably higher than DRM [209–212]. Two different mechanisms were proposed, i.e. (i)  $\text{CH}_x$  generated from the decomposition of  $\text{C}_2\text{H}_6$  reacting with the absorbed oxygen to form  $\text{CH}_x\text{O}$ , which decomposes to produce CO and  $\text{H}_2$  [209–211, 213], and (ii)  $\text{CO}_2$  and  $\text{H}_2$  reacting to form hydroxyl species, which subsequently react with  $\text{CH}_x$  [214, 215].

The yield and selectivity in dry reforming of propane also depended on the catalysts used. When a series of noble metals were supported on  $\text{Al}_2\text{O}_3$ , the reactivity order was shown as  $\text{Ru} > \text{Rh}$ ,  $\text{Pd} > \text{Pt}$ , Ir. Among them,  $\text{Ru}/\text{Al}_2\text{O}_3$  exhibited the highest  $\text{H}_2$  selectivity. As for the support activity with Rh as the active metal,  $\text{Al}_2\text{O}_3$  performed the best, followed by  $\text{TiO}_2$ ,  $\text{MgO}$ , and  $\text{SiO}_2$  [209–211]. In addition to noble metals, Ni supported on Mg and Al support derived from a hydrotalcite precursor presented excellent stability due to the continuous supply of oxygen from  $\text{CO}_2$  to Ni metal [216].

Other hydrocarbons such as *n*-butane, *iso*-butane, *neo*-pentane, *n*-heptane, ethylene, and *n*-dodecane could be converted to syngas, short hydrocarbon molecules, and coke when  $\text{CO}_2$  was fed into the reactor. MnO exhibited high catalytic performance, especially when promoted by Cr and K and supported on  $\text{La}_2\text{O}_3$  and  $\text{ZrO}_2$ . Similarly, Ni or Rh as the active metals performed well in heavier hydrocarbon dry reforming reactions [208, 213, 217, 218].

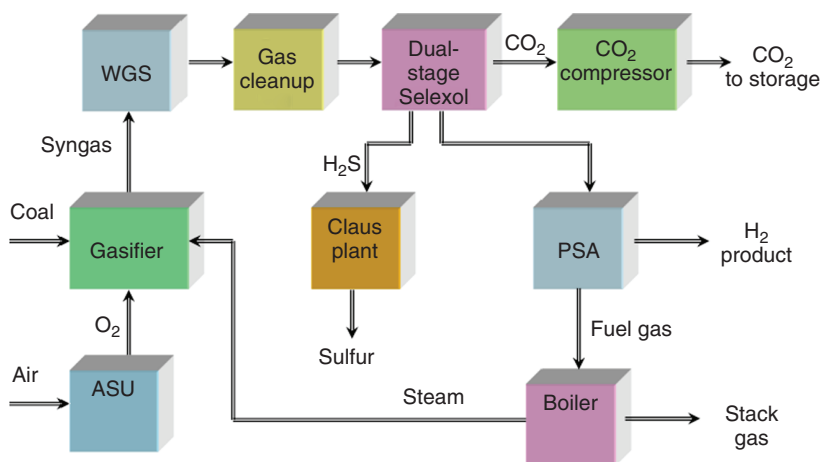


**Figure 1.11** A simplified block diagram of a coal gasification hydrogen plant with  $\text{CO}_2$  capture. ASU; air separation unit. Source: Reproduced with permission from Muradov [1]: © 2017, Elsevier.

Besides the reforming of hydrocarbons, coal gasification was another pathway to generate hydrogen gas, where coal reacted with an  $O_2$ -steam mixture at high temperature [219]. Despite the low hydrogen content ( $H/C = 0.1$ ), the specific importance of integrated gasification cycle lies in the simultaneous production of hydrogen gas and electricity [1]. As shown in Figure 1.11, the produced syngas flowed into a WGS reactor with a sulfur-tolerant catalyst to produce a  $H_2$ - $CO_2$  mixture. Then, a double-stage Selexol unit was equipped to remove the  $H_2S$  and  $CO_2$ , generating an acidic gas-free stream that was directed to PSA for  $H_2$  purification [220].

## 1.2 Conclusions and Prospects

In this chapter, we summarized the catalytic routes for production of hydrogen gas, by converting fossil fuels such as methane. Both the reaction mechanisms and values of the reactions are included. To realize a more efficient and cost-effective industry process, we have covered the recent progress of catalyst design for each reaction.

The main routes of hydrogen production are still those related to the catalytic processing of methane. Among the several approaches, methane decomposition is still at the lab scale and work has to explore the way to industrialization. SRM is dominant in producing hydrogen gas, along with ATR and POM as the efficient and economical technologies for the large-scale production of hydrogen gas. Furthermore, due to the increasing concern toward environmental issues, DRM attracts much attention. To further enhance the catalytic performance and stability, it is necessary to modify the catalysts using promoters, dopants, novel architectures, and regulated morphologies and structures. Besides, operation parameters and reactor designs can be further refined to meet industry requirements.

In addition to the issues above, advanced characterization methods and simulation techniques are needed to elucidate mechanisms of catalyst formation, the interaction between the catalyst and the reactant, and the kinetics. Moreover, it is crucial and urgent to refine the existing “good” catalysts at the lab-scale level to be capable at industry level where the mass diffusion and energy transfer are both different from the lab experiments. In the meanwhile, optimization of the existing industry system and parameters should also be considered.

## References

- 1 Muradov, N. (2017). *Int. J. Hydrogen Energy* 42: 14058–14088.
- 2 Navarro, R., Pena, M., and Fierro, J. (2007). *Chem. Rev.* 107: 3952–3991.
- 3 International Energy Agency (2007). *Hydrogen Production and Distribution: IEA Energy Technology Essentials*. Paris: OECD/IEA.
- 4 Ball, M. and Wietschel, M. (2009). *Int. J. Hydrogen Energy* 34: 615–662.
- 5 Balat, M. and Balat, M. (2009). *Int. J. Hydrogen Energy* 34: 3589–3603.
- 6 Ong, H., Mahlia, T., and Masjuki, H. (2011). *Renew. Sustain. Energy Rev.* 15: 639–647.

- 7 Wang, Q., Chen, X., Jha, A.N., and Rogers, H. (2014). *Renew. Sustain. Energy Rev.* 30: 1–28.
- 8 Konieczny, A., Mondal, K., Wiltowski, T., and Dydo, P. (2008). *Int. J. Hydrogen Energy* 33: 264–272.
- 9 Ashik, U.P.M., Daud, W.M.A.W., and Abbas, H.F. (2015). *Renew. Sustain. Energy Rev.* 44: 221–256.
- 10 Voldsund, M., Jordal, K., and Anantharaman, R. (2016). *Int. J. Hydrogen Energy* 41: 4969–4992.
- 11 Ball, M. and Weeda, M. (2015). *Int. J. Hydrogen Energy* 40: 7903–7919.
- 12 Zhang, J.B., Li, X., Chen, H.Y. et al. (2017). *Int. J. Hydrogen Energy* 42: 19755–19775.
- 13 Gaudernack, B. (1998). Hydrogen production from fossil fuels. In: *Hydrogen Power: Theoretical and Engineering Solutions* (ed. T.O. Saetre), 75–89. Netherlands: Springer.
- 14 Muradov, N. (2002). Hydrogen from fossil fuels without CO<sub>2</sub> emissions. In: *Advances in Hydrogen Energy* (ed. P.C.E. Grégoire and F. Lau), 1–16. USA: Springer.
- 15 Teo, K.B., Singh, C., Chhowalla, M., and Milne, W.I. (2003). Catalytic synthesis of carbon nanotubes and nanofibers. In: *Encyclopedia of Nanoscience and Nanotechnology*, vol. 10 (ed. H.S. Nalwa), 1–22. USA: American Scientific Publishers.
- 16 Baharudin, L. and Watson, M.J. (2018). *Rev. Chem. Eng.* 34: 43–72.
- 17 Lobo, L. and Trimm, D. (1973). *J. Catal.* 29: 15–19.
- 18 Robertson, S. (1972). *Carbon* 10: 221–229.
- 19 Bayat, N., Rezaei, M., and Meshkani, F. (2016). *Korean J. Chem. Eng.* 33: 490–499.
- 20 Ibrahim, A.A., Fakeeha, A.H., Al-Fatesh, A.S. et al. (2015). *Int. J. Hydrogen Energy* 40: 7593–7600.
- 21 Aiello, R., Fiscus, J., Loye, H., and Amiridis, M. (2000). *Appl. Catal., A* 192: 227–234.
- 22 Bayat, N., Rezaei, M., and Meshkani, F. (2016). *Int. J. Hydrogen Energy* 41: 1574–1584.
- 23 Bayat, N., Meshkani, F., and Rezaei, M. (2016). *Int. J. Hydrogen Energy* 41: 13039–13049.
- 24 Lua, A.C. and Wang, H.Y. (2014). *Appl. Catal., B* 156: 84–93.
- 25 Awadallah, A.E. and Aboul-Enein, A.A. (2015). *Egypt. J. Pet.* 24: 299–306.
- 26 Yu, Y., Cui, M.S., Li, M.L. et al. (2014). *J. Rare Earths* 32: 709–714.
- 27 Liu, F., Chen, L., Yang, L. et al. (2016). *Int. J. Hydrogen Energy* 41: 4592–4602.
- 28 Kim, M., Lee, E., Jun, J. et al. (2004). *Int. J. Hydrogen Energy* 29: 187–193.
- 29 Bai, Z., Chen, H., Li, B., and Li, W. (2005). *J. Anal. Appl. Pyrolysis* 73: 335–341.
- 30 Moliner, R., Suelves, I., Lazaro, M., and Moreno, O. (2005). *Int. J. Hydrogen Energy* 30: 293–300.
- 31 Shen, Y. and Lua, A.C. (2016). *J. Colloid Interface Sci.* 462: 48–55.
- 32 Serrano, D., Botas, J., Pizarro, P. et al. (2008). *Chem. Commun.* 6585–6587.
- 33 Dunker, A., Kumar, S., and Mulawa, P. (2006). *Int. J. Hydrogen Energy* 31: 473–484.

- 34 Serrano, D., Botas, J., and Guil-Lopez, R. (2009). *Int. J. Hydrogen Energy* 34: 4488–4494.
- 35 Muradov, N., Smith, F., Bockerman, G., and Scammon, K. (2009). *Appl. Catal., A* 365: 292–300.
- 36 Dufour, A., Celzard, A., Fierro, V. et al. (2008). *Appl. Catal., A* 346: 164–173.
- 37 Muradov, N., Chen, Z., and Smith, F. (2005). *Int. J. Hydrogen Energy* 30: 1149–1158.
- 38 Chaubey, R., Sahu, S., James, O.O., and Maity, S. (2013). *Renew. Sustain. Energy Rev.* 23: 443–462.
- 39 Pantaleo, G., La Parola, V., Deganello, F. et al. (2015). *Appl. Catal., B* 164: 135–143.
- 40 Pal, P., Singha, R.K., Saha, A. et al. (2015). *J. Phys. Chem. C* 119: 13610–13618.
- 41 Bi, X.-J., Hong, P.-J., Xie, X.-G., and Dai, S.-S. (1999). *React. Kinet. Catal. Lett.* 66: 381–386.
- 42 Abbasi, R., Huang, G., Istratescu, G.M. et al. (2015). *Can. J. Chem. Eng.* 93: 1474–1482.
- 43 Santis-Alvarez, A.J., Büchel, R., Hild, N. et al. (2014). *Appl. Catal., A* 469: 275–283.
- 44 Staniforth, J., Evans, S.E., Good, O.J. et al. (2014). *Dalton Trans.* 43: 15022–15207.
- 45 Meng, B., Zhang, H., Zhao, Z. et al. (2016). *Catal. Today* 259: 388–392.
- 46 Ji, Y., Li, W., Xu, H., and Chen, Y. (2001). *Catal. Lett.* 71: 45–48.
- 47 Wang, H.Y. and Ruckenstein, E. (2001). *Catal. Lett.* 75: 13–18.
- 48 Yang, S., Kondo, J.N., Hayashi, K. et al. (2004). *Appl. Catal., A* 277: 239–246.
- 49 Wang, H.Y. and Ruckenstein, E. (2001). *J. Catal.* 199: 309–317.
- 50 Wang, H.-T., Li, Z.-H., and Tian, S.-X. (2004). *React. Kinet. Catal. Lett.* 83: 245–252.
- 51 González, M.G., Nichio, N.N., Moraweck, B., and Martin, G. (2000). *Mater. Lett.* 45: 15–18.
- 52 Basile, F., Fornasari, G., Trifirò, F., and Vaccari, A. (2001). *Catal. Today* 64: 21–30.
- 53 Zhu, Y., Zhang, S., Shan, J.-J. et al. (2013). *ACS Catal.* 3: 2627–2639.
- 54 Ding, C., Ai, G., Zhang, K. et al. (2015). *Int. J. Hydrogen Energy* 40: 6835–6843.
- 55 Chalupka, K.A., Jozwiak, W.K., Rynkowski, J. et al. (2014). *Appl. Catal., B* 146: 227–236.
- 56 Yan, Q.G., Weng, W.Z., Wan, H.L. et al. (2003). *Appl. Catal., A* 239: 43–58.
- 57 Brackmann, R., Perez, C.A., and Schmal, M. (2014). *Int. J. Hydrogen Energy* 39: 13991–14007.
- 58 Yoon, J.S., Lim, Y.-S., Choi, B.H., and Hwang, H.J. (2014). *Int. J. Hydrogen Energy* 39: 7955–7962.
- 59 Morales, M., Espiell, F., and Segarra, M. (2014). *Int. J. Hydrogen Energy* 39: 6454–6461.
- 60 Sengodan, S., Lan, R., Humphreys, J. et al. (2018). *Renew. Sustain. Energy Rev.* 82: 761–780.
- 61 Abad, A.V. and Dodds, P.E. (2017). *Production of Hydrogen*, vol. 3. Elsevier.
- 62 Acar, C. and Dincer, I. (2013). *Int. J. Hydrogen Energy* 39: 1–12.

- 63 Akamatsu, K., Murakami, T., Sugawara, T. et al. (2011). *AlChE J.* 57: 1882–1888.
- 64 Iulianelli, A., Liguori, S., Wilcox, J., and Basile, A. (2016). *Catal. Rev.* 58: 1–35.
- 65 Utaka, T., Sekizawa, K., and Eguchi, K. (2000). *Appl. Catal., A* 194–195: 21–26.
- 66 Ginés, M.J.L., Amadeo, N., Laborde, M., and Apesteguía, C.R. (1995). *Appl. Catal., A* 131: 283–296.
- 67 Ji, G.Z., Yao, J.G., Clough, P.T. et al. (2018). *Energy Environ. Sci.* 11: 2647–2672.
- 68 Collodi, G. (2010). Hydrogen production via steam reforming with CO<sub>2</sub> capture. <http://www.audic.it/CICAP4/webpapers/7Collodi.pdf>.
- 69 Angeli, S.D., Monteleone, G., Giaconia, A., and Lemonidou, A.A. (2014). *Int. J. Hydrogen Energy* 39: 1979–1997.
- 70 Roy, P.S., Park, N.-K., and Kim, K. (2014). *Int. J. Hydrogen Energy* 39: 4299–4310.
- 71 Simakov, D.S.A., Luo, H.Y., and Román-Leshkov, Y. (2015). *Appl. Catal., B* 168–169: 540–549.
- 72 Cassinelli, W.H., Damyanova, S., Parizotto, N.V. et al. (2014). *Appl. Catal., A* 475: 256–269.
- 73 Xue, X. and Wu, S. (2015). *Int. J. Hydrogen Energy* 40: 5617–5623.
- 74 Zhang, Y., Wang, W., Wang, Z. et al. (2015). *Catal. Today* 256: 130–136.
- 75 Khzouz, M., Wood, J., Pollet, B., and Bujalski, W. (2013). *Int. J. Hydrogen Energy* 38: 1664–1675.
- 76 Andrade, M.L., Almeida, L., do Carmo Rangel, M. et al. (2014). *Chem. Eng. Technol.* 37: 343–348.
- 77 Amjad, U., Gonçalves, G., Camargo Fernandes-Machado, N.R.C., and Specchia, S. (2015). *Catal. Today* 257: 122–130.
- 78 Nikolla, E., Schwank, J., and Linic, S. (2009). *J. Catal.* 263: 220–227.
- 79 Choi, S.O. and Moon, S.H. (2009). *Catal. Today* 146: 148–153.
- 80 Urasaki, K., Sekine, Y., Kawabe, S. et al. (2005). *Appl. Catal., A* 286: 23–29.
- 81 Wang, Z., Shao, X., Hu, X. et al. (2014). *Catal. Today* 228: 199–205.
- 82 Krumpelt, M., Krause, T.R., Carter, J.D. et al. (2002). *Catal. Today* 77: 3–16.
- 83 Ma, R.S., Xu, B., and Zhang, X. (2019). *Catal. Today* 338: 18–30.
- 84 Horn, R. and Schlögl, R. (2015). *Catal. Lett.* 145: 23–39.
- 85 Dybkjær, I. (1995). *Fuel Process. Technol.* 42: 85–107.
- 86 Bharadwaj, S. and Schmidt, L. (1995). *Fuel Process. Technol.* 42: 109–127.
- 87 Aasberg-Petersen, K. and Christensen, T.S. (2004). Synthesis gas production for FT synthesis. In: *Fischer–Tropsch Technology* (ed. A. Steynberg and M. Dry), 258–352. Amsterdam: Elsevier.
- 88 Bellows, R.J. (1999). Technical challenges for hydrocarbon fuel reforming. In: *Proceedings of the joint DOE/ONR FuelCell workshop*, Baltimore, 6.
- 89 Lisboa, J.S., Terra, L.E., Silva, P.R.J. et al. (2011). *Fuel Process. Technol.* 92: 2075–2082.
- 90 Roh, H.-S., Jun, K.-W., Dong, W.-S. et al. (2001). *Catal. Lett.* 74: 31–36.
- 91 Dantas, S.C., Escritori, J.C., Soares, R.R., and Hori, C.E. (2010). *Chem. Eng. J.* 156: 380–387.
- 92 Cao, L., Pan, L., Ni, C. et al. (2010). *Fuel Process. Technol.* 91: 306–312.

- 93 Ruiz, J.A.C., Passos, F.B., Bueno, J.M.C. et al. (2008). *Appl. Catal. A* 334: 259–267.
- 94 Escritori, J.C., Dantas, S.C., Soares, R.R., and Hori, C.E. (2009). *Catal. Commun.* 10: 1090–1094.
- 95 Cai, X., Dong, X., Lin, W., and Nat, J. (2006). *Gas Chem.* 15: 122–126.
- 96 Elvidge, C.D., Bazilian, M.D., Zhizhin, M. et al. (2018). *Energy Strateg. Rev.* 20: 156–162.
- 97 Song, C., Liu, Q., Ji, N. et al. (2018). *Renew. Sustain. Energy Rev.* 82: 215–231.
- 98 Zain, M.M. and Mohamed, A.R. (2018). *Renew. Sustain. Energy Rev.* 98: 56–63.
- 99 Paksoy, A.I., Selen, B., and Aksoylu, A.E. (2015). *Appl. Catal., B* 168–169: 164–174.
- 100 Bian, Z.F., Das, S., Wai, M.H. et al. (2017). *ChemPhysChem* 18: 3117–3134.
- 101 Li, Z.W., Li, M., Bian, Z.F. et al. (2016). *Appl. Catal., B* 188: 324–341.
- 102 Kathiraser, Y., Oemar, U., Saw, E.T. et al. (2015). *Chem. Eng. J.* 278: 62–78.
- 103 Bian, Z.F. and Kawi, S. (2020). *Catal. Today* 339: 3–23.
- 104 Kawi, S., Kathiraser, Y., Ni, J. et al. (2015). *ChemSusChem* 8: 3556–3575.
- 105 Li, Z.W., Das, S., Hongmanorom, P. et al. (2018). *Catal. Sci. Technol.* 8: 2763–2778.
- 106 Bradford, M.C.J. and Vannice, M.A. (1996). *Appl. Catal. A* 142: 73–96.
- 107 Gadalla, A.M. and Bower, B. (1988). *Chem. Eng. Sci.* 43: 3049–3062.
- 108 Chubb, T.A. (1980). *Sol. Energy* 24: 342–345.
- 109 McCrary, J.H., McCrary, C.E., Clark, D.H., and Chubb, T.A. (1980). *Proc. Meet. Am. Sect. Int. Sol. Eng. Soc.* 3: 99–103.
- 110 McCrary, J.H., McCrary, G.E., Chubb, T.A. et al. (1982). *Sol. Energy* 29: 141–151.
- 111 Peral, J.M.A. (1986). *Proc. Intersoc. Energy Convers. Engng Conf.* 21: 695–701.
- 112 Jang, W.-J., Shim, J.-O., Kim, H.-M. et al. (2019). *Catal. Today* 324: 15–26.
- 113 Abdulrasheed, A., Jalil, A.A., Gambo, Y. et al. (2019). *Renew. Sustain. Energy Rev.* 108: 175–193.
- 114 Gould, T.D., Izar, A., Weimer, A.W. et al. (2014). *ACS Catal.* 4: 2714–2717.
- 115 Xie, X., Otremba, T., Littlewood, P. et al. (2013). *ACS Catal.* 3: 224–229.
- 116 Lavoie, J.-M. (2014). *Front. Chem.* 2: 1–17.
- 117 Von der Assen, N., Voll, P., Peters, M., and Bardow, A. (2014). *Chem. Soc. Rev.* 43: 7982–7994.
- 118 Singh, R., Dhir, A., Mohapatra, S.K., and Mahla, S.K. (2020). *Biomass Convers. Biorefin.* 10: 567–587.
- 119 Rostrup-Nielsen, J. and Hansen, J.-H. (1993). *J. Catal.* 144: 38–49.
- 120 Bradford, M.C.J. and Vannice, M.A. (1998). *J. Catal.* 173: 157–171.
- 121 Van Santen, R.A. and Neurock, M. (1995). *Catal. Rev. Sci. Eng.* 37: 557–698.
- 122 Koster, A.D.E. and van Santen, R.A. (1991). *J. Catal.* 127: 141–166.
- 123 Bitter, J.H., Hally, W., Seshan, K. et al. (1996). *Catal. Today* 29: 349–353.
- 124 Roberts, S. and Gorte, R.J. (1991). *J. Phys. Chem.* 95: 5600–5604.
- 125 van Keulen, A.N.J., Seshan, K., Hoebink, J.H.B.J., and Ross, J.R.H. (1997). *J. Catal.* 166: 306–314.

- 126 Wittich, K., Krämer, M., Bottke, N., and Schunk, S.A. (2020). *ChemCatChem* 12: 2130–2147.
- 127 Ruckenstein, E. and Wang, H.Y. (2000). *Appl. Catal. A* 204: 257–263.
- 128 Stevenson, S.A., Dumesic, J.A., Baker, R.T.K., and Ruckenstein, E. (ed.) (1987). *Metal-Support Interactions in Catalysis, Sintering, and Redispersion*, 141. New York: Van Nostrand Reinhold.
- 129 Ni, J., Zhao, J., Chen, L.W. et al. (2016). *ChemCatChem* 8: 3732–3739.
- 130 Wang, C., Sun, N., Kang, M. et al. (2013). *Catal. Sci. Technol.* 3: 2435–2443.
- 131 Al-Fatesh, A.S., Arafat, Y., Atia, H. et al. (2017). *J. CO<sub>2</sub> Util.* 21: 395–404.
- 132 Phan, T.S., Sane, A.R., de Vasconcelos, B.R. et al. (2018). *Appl. Catal., B* 224: 310–321.
- 133 Zhang, L., Lian, J., Li, L. et al. (2018). *Microporous Mesoporous Mater.* 266: 189–197.
- 134 Li, X.Y., Li, D., Tian, H. et al. (2017). *Appl. Catal., B* 202: 683–694.
- 135 Zhang, Z., Verykios, X.E., MacDonald, S., and Affrossman, S. (1996). *J. Phys. Chem.* 100: 744–752.
- 136 Ni, J., Chen, L.W., Lin, J.Y. et al. (2013). *Int. J. Hydrogen Energy* 38: 13631–13642.
- 137 Li, K., He, F., Yu, H.M. et al. (2018). *J. Catal.* 364: 248–261.
- 138 Pan, Y.-X., Kuai, P., Liu, Y. et al. (2010). *Energy Environ. Sci.* 3: 1322–1325.
- 139 Dębek, R., Motak, M., Galvez, M.E. et al. (2017). *Int. J. Hydrogen Energy* 42: 1–12.
- 140 Świrk, K., Gálvez, M.E., Motak, M. et al. (2018). *J. CO<sub>2</sub> Util.* 27: 247–258.
- 141 Ni, J., Chen, L., Lin, J., and Kawi, S. (2012). *Nano Energy* 1: 674–686.
- 142 Liu, Z.Y., Grinter, D.C., Lustemberg, P.G. et al. (2016). *Angew. Chem. Int. Ed.* 55: 7455–7459.
- 143 Macario, A., Frontera, P., Candamano, S. et al. (2019). *J. Nanosci. Nanotechnol.* 19: 3135–3147.
- 144 Lian, Z., Olanrele, S.O., Si, C.W. et al. (2020). *J. Phys. Chem. C* 124: 5118–5124.
- 145 Horváth, A., Stefler, G., Geszti, O. et al. (2011). *Catal. Today* 169: 102–111.
- 146 Safavinia, B., Wang, Y.M., Jiang, C.Y. et al. (2020). *ACS Catal.* 10: 4070–4079.
- 147 Oemar, U., Hidajat, K., and Kawi, S. (2011). *Appl. Catal., A* 402: 176–187.
- 148 Sutthiumporn, K. and Kawi, S. (2011). *Int. J. Hydrogen Energy* 36: 14435–14446.
- 149 Yang, W.Q., Wang, Z.B., Tan, W.Z. et al. (2020). *Sci. China Mater.* 63: 364–374.
- 150 Lou, Y., Steib, M., Zhang, Q. et al. (2017). *J. Catal.* 356: 147–156.
- 151 Wang, Y., Yao, L., Wang, Y. et al. (2018). *ACS Catal.* 8: 6495–6506.
- 152 Liu, W.M., Li, L., Zhang, X.H. et al. (2018). *J. CO<sub>2</sub> Util.* 27: 297–307.
- 153 Sun, N., Wen, X., Wang, F. et al. (2011). *Appl. Surf. Sci.* 257: 9169–9176.
- 154 Kang, D., Lim, H.S., Lee, M., and Lee, J.W. (2018). *Appl. Energy* 211: 174–186.
- 155 Fan, M.S., Abdullah, A.Z., and Bhatia, S. (2009). *ChemCatChem* 1: 192–208.
- 156 Pakhare, D., Schwartz, V., Abdelsayed, V. et al. (2014). *J. Catal.* 316: 78–92.
- 157 Wang, H.Q., Dong, X.L., Zhao, T.T. et al. (2019). *Appl. Catal., B* 245: 302–313.
- 158 Yang, E.H., Noh, Y.S., Hong, G.H., and Moon, D.J. (2018). *Catal. Today* 299: 242–250.

- 159 Rynkowski, J., Samulkiewicz, P., Ladavos, A., and Pomonis, P. (2004). *Appl. Catal., A* 263: 1–9.
- 160 Sutthiumporn, K., Maneerung, T., Kathiraser, Y., and Kawi, S. (2012). *Int. J. Hydrogen Energy* 37: 11195–11207.
- 161 Ruckenstein, E. and Hu, Y.H. (1996). *J. Catal.* 162: 230–238.
- 162 Foley, H.C., Hong, A.J., Brinen, J.S. et al. (1990). *Appl. Catal.* 61: 351–375.
- 163 Lee, J.H., Lee, E.G., Joo, O.S., and Jung, K.D. (2004). *Appl. Catal., A* 269: 1–6.
- 164 Fan, M.S., Abdullah, A.Z., and Bhatia, S. (2011). *ChemSusChem* 4: 1643–1653.
- 165 Kambolis, A., Matralis, H., Trovarelli, A., and Papadopoulou, C. (2010). *Appl. Catal., A* 377: 16–26.
- 166 Li, L., Zhou, L., Ould-Chikh, S. et al. (2015). *ChemCatChem* 7: 819–829.
- 167 Li, Z., Kathiraser, Y., and Kawi, S. (2015). *ChemCatChem* 7: 160–168.
- 168 Gao, X.Y., Hidajat, K., and Kawi, S. (2016). *J. CO<sub>2</sub> Util.* 15: 146–153.
- 169 García-Vargas, J.M., Valverde, J.L., Lucas-Consuegra, A.D. et al. (2013). *Int. J. Hydrogen Energy* 38: 4524–4532.
- 170 Tomishige, K., Yamazaki, O., Chen, Y.G. et al. (1998). *Catal. Today* 45: 35–39.
- 171 Horváth, A., Gucci, L., Kocsonya, A. et al. (2013). *Appl. Catal., A* 468: 250–259.
- 172 Li, Y.M., Wang, Z.J., Zhang, B. et al. (2020). *Catalysts* 10: 501.
- 173 Wang, H.Q., Han, J., Zhao, B. et al. (2019). *Mol. Catal.* 475: 110486.
- 174 Zhang, Q., Zhang, T., Shi, Y. et al. (2017). *J. CO<sub>2</sub> Util.* 17: 10–19.
- 175 Zhang, Q.L., Sun, M.H., Ning, P. et al. (2019). *Appl. Surf. Sci.* 469: 368–377.
- 176 Kang, D., Lim, H.S., and Lee, J.W. (2017). *Int. J. Hydrogen Energy* 42: 11270–11282.
- 177 Baktash, E., Littlewood, P., Pfrommer, J. et al. (2015). *ChemCatChem* 7: 1280–1284.
- 178 Qian, L., Huang, K., Wang, H. et al. (2017). *Microporous Mesoporous Mater.* 243: 301–310.
- 179 Wang, M., Zhang, Q., Zhang, T. et al. (2017). *Chem. Eng. J.* 313: 1370–1381.
- 180 Xu, L., Song, H., and Chou, L. (2011). *Appl. Catal., B* 108–109: 177–190.
- 181 Xu, L., Song, H., and Chou, L. (2012). *Int. J. Hydrogen Energy* 37: 18001–18020.
- 182 Xu, L., Miao, Z., Song, H. et al. (2014). *Catal. Sci. Technol.* 4: 1759–1770.
- 183 Ashcroft, A.T., Cheetham, A.K., Green, M.L.H., and Vernon, P.D.F. (1991). *Nature* 352: 225–226.
- 184 Wang, N., Xu, Z., Deng, J. et al. (2014). *ChemCatChem* 6: 1470–1480.
- 185 Yin, Y., Rioux, R.M., Erdonmez, C.K. et al. (2004). *Science* 304: 711–714.
- 186 Park, J.C., Bang, J.U., Lee, J. et al. (2010). *J. Mater. Chem.* 20: 1239–1246.
- 187 Kim, D.H., Kim, S.Y., Han, S.W. et al. (2015). *Appl. Catal., A* 495: 184–191.
- 188 Lu, Y., Guo, D., Ruan, Y.Z. et al. (2018). *J. CO<sub>2</sub> Util.* 24: 190–199.
- 189 Li, Z.W. and Kawi, S. (2018). *ChemCatChem* 10: 2994–3001.
- 190 Cao, Y., Lu, M.R., Fang, J.H. et al. (2017). *Chem. Commun.* 53: 7549–7552.
- 191 Tian, J.Q., Ma, B., Bu, S.Y. et al. (2018). *Chem. Commun.* 54: 13993–13996.
- 192 Dou, J., Zhang, R.G., Hao, X.B. et al. (2019). *Appl. Catal., B* 254: 612–623.
- 193 Bian, Z.F. and Kawi, S. (2018). *ChemCatChem* 10: 320–328.
- 194 Li, Z., Mo, L., Kathiraser, Y., and Kawi, S. (2014). *ACS Catal.* 4: 1526–1536.
- 195 Li, Z.W., Kathiraser, Y., Ashok, J. et al. (2014). *Langmuir* 30: 14694–14705.

- 196 Bian, Z.F., Suryawinata, I.Y., and Kawi, S. (2016). *Appl. Catal., B* 195: 1–8.
- 197 Du, X., Zhang, D., Gao, R. et al. (2013). *Chem. Commun.* 49: 6770–6772.
- 198 Ahmed, K., Gamman, J., and Föger, K. (2002). *Solid State Ionics* 152–153: 485–492.
- 199 Wang, X. and Gorte, R.J. (2002). *Appl. Catal., A* 224: 209–218.
- 200 Suzuki, T., Iwanami, H.-I., Iwamoto, O., and Kitahara, T. (2001). *Int. J. Hydrogen Energy* 26: 935–940.
- 201 Laosiripojana, N. and Assabumrungrat, S. (2006). *J. Power Sources* 158: 1348–1357.
- 202 Ramírez-Cabrera, E., Atkinson, A., and Chadwick, D. (2004). *Appl. Catal., B* 47: 127–131.
- 203 Fornasiero, P., Balducci, G., Monte, R.D. et al. (1996). *J. Catal.* 164: 173–183.
- 204 Miki, T., Ogawa, T., Haneda, M. et al. (1990). *J. Phys. Chem.* 94: 6464–6467.
- 205 Imamura, S., Shono, M., Okamoto, N. et al. (1996). *Appl. Catal., A* 142: 279–288.
- 206 Kacimi, S., Barbier, J. Jr., Taha, R., and Duperz, D. (1993). *Catal. Lett.* 22: 343–350.
- 207 Pijolat, M., Prin, M., and Soustelle, M. (1995). *J. Chem. Soc., Faraday Trans.* 91: 3941–3948.
- 208 Krylov, O.V., Mamedov, A.K., and Mirzabekova, S.R. (1995). *Ind. Eng. Chem. Res.* 34: 474–482.
- 209 Solymosi, F., Tolmács, P., and Kedves, K. (2003). *J. Catal.* 216: 377–385.
- 210 Solymosi, F. and Tolmács, P. (2002). *Catal. Lett.* 83: 183–186.
- 211 Solymosi, F., Szőke, A., and Ovári, L. (1999). *J. Catal.* 186: 269–278.
- 212 Futamura, S., Kabashima, H., and Einaga, H. (2004). *IEEE Trans. Ind. Appl.* 40: 1476–1481.
- 213 Puolakka, J. (2007). *CO<sub>2</sub> reforming; Thesis for the Degree of Licentiate of Science and Technology*. Helsinki, Finland: Helsinki University of Technology.
- 214 Bradford, M.C.J. and Vannice, M.A. (1996). *Appl. Catal. A* 142: 97–122.
- 215 Bradford, M.C.J. and Vannice, M.A. (1999). *Catal. Rev. Sci. Eng.* 41: 1–42.
- 216 Olafsen, C., Daniel, Y., Schuarman, L. et al. (2006). *Catal. Today* 115: 179–185.
- 217 Mirzabekova, S.R., Farkhadovs, G.T., Mamedov, A.K., and Rustamov, M.I. (1993). *Kinet. Catal.* 34: 841–843.
- 218 Fujimura, S., Nakagawa, K., Ikenaga, N., and Suzuki, T. (1997). *Sekiyu Gakkaishi* 40: 179–184.
- 219 Wang, H., Huang, H., Xue, D., and Ouyang, M. (2013). Hydrogen and fuel-cell vehicle technology. In: *Sustainable Automotive Energy System in China*, 301–333. Berlin, Heidelberg: Springer.
- 220 US DOE National Energy Technology Laboratory. (2010). Assessment of Hydrogen Production with CO<sub>2</sub> Capture Volume 1: Baseline State-of-the-Art Plants. DOE/NETL Final report 2010/1434.